Available online at www.sciencedirect.com

ScienceDirect

Geochimica et Cosmochimica Acta 314 (2021) 358–380

Geochimica et Cosmochimica Acta

www.elsevier.com/locate/gca

Geochronology of mafic magmatism and hydrothermal alteration during early stages of South Atlantic opening

Karine Zuccolan Carvas [a,*], Paulo Marcos de Paula Vasconcelos [b], Leila Soares Marques [a], Teresa Ubide [b], Isabela de Oliveira Carmo [c], Marly Babinski [d]

[a] *Instituto de Astronomia, Geofísica e Ciências Atmosféricas, Universidade de São Paulo, São Paulo, SP 05508-090, Brazil*
[b] *School of Earth and Environmental Sciences, The University of Queensland, Brisbane, QLD 4072, Australia*
[c] *PETROBRAS/CENPES, Rio de Janeiro, RJ 21941-915, Brazil*
[d] *Instituto de Geociências, Universidade de São Paulo, São Paulo, SP 05422-970, Brazil*

Received 29 March 2021; accepted in revised form 16 August 2021; Available online 23 August 2021

Abstract

$^{40}Ar/^{39}Ar$ laser incremental-heating geochronology of whole-rock fragments and minerals from primitive subalkaline mafic dykes from the Cabo Frio Tectonic Domain, southeastern Brazil, reveals a complex combination of intrusive ages, apparent ages affected by excess argon, and ages that record late-stage hydrothermal alteration. Incremental-heating analysis of encapsulated magmatic amphibole-biotite clusters reveals a minimum intrusive age of 132.83 ± 0.30 Ma. Sericitized plagioclase crystals show the percolation of K-rich fluids at ~106 Ma. Albitized plagioclase phenocrysts suggest the percolation of Na-rich fluids in the 60–30 Ma interval. Hydrothermal alteration events overlap in time with pulses of alkaline magmatism in the extending Brazilian crust, suggesting a link between magmatic activity and generation of fluid circulation cells along the margin and adjacent sedimentary basins. Evidence for pervasive hydrothermal re-setting of the K-Ar system in the Cabo Frio Tectonic Domain dykes suggests that young $^{40}Ar/^{39}Ar$ geochronology results obtained for mafic dykes here and elsewhere along the continental margins may not record multiple intrusive events, reflecting instead partial or total resetting of the K-Ar system by water-rock interaction during fluid circulation.

Keywords: South Atlantic opening; Hydrothermalism during continental rifting; Cretaceous tholeiitic magmatism; $^{40}Ar/^{39}Ar$ geochronology of mafic dykes; Effects of hydrothermalism in whole rock geochemistry

1. INTRODUCTION

Continental rifts are invariably accompanied by intrusive mafic magmatism, often in the form of dyke swarms, which play an important role in fault reactivation and crustal accretion during plate divergence (Thybo and Nielsen, 2009; Rivalta et al., 2015). By generating or reactivating zones of weaknesses in the crust, dykes affect the rheological behavior of the lithosphere (Lavecchia et al., 2016; and references therein). Dyke swarms ascend through pathways that facilitate magma supply to major extrusive events that accompany continental break-up. To reconstruct the relationship between intrusive mafic magmatism, extrusive magmatism, and continental rifting, information on depth, temperature, source, duration, and rate of magma emplacement is necessary. Acquiring that information is not trivial, however.

* Corresponding author.
E-mail addresses: karine.carvas@iag.usp.br (K.Z. Carvas), p.vasconcelos@uq.edu.au (P.M.P. Vasconcelos), leila.marques@usp.br (L.S. Marques), t.ubide@uq.edu.au (T. Ubide), icarmo@petrobras.com.br (I.O. Carmo), babinski@ usp.br (M. Babinski).

https://doi.org/10.1016/j.gca.2021.08.017
0016-7037/

$^{40}Ar/^{39}Ar$ geochronology is one of the most commonly applied dating methods to obtain the ages of mafic dykes (McDougall and Harrison, 1999). It has been widely applied to date dykes associated with the Paraná-Etendeka Magmatic Province, but $^{40}Ar/^{39}Ar$ results from aphanitic dykes are often compromised by the presence of excess argon in whole-rock analyses; results for porphyritic dykes often suggest that the phenochrysts are altered (Gomes and Vasconcelos, 2021). The preferential emplacement of dykes along deep faults prevents magmatic degassing and promotes the incorporation of excess argon; however, when reaching shallower levels, these faults focus fluid migration, promoting fluid-rock interaction and partially modifying the isotopic and geochemical signatures of the dykes (e.g., Kempe et al., 2015). We will show here that mafic dykes associated with Gondwana rifting and opening of the South Atlantic Ocean (Fig. 1) are marred by both of these difficulties. We will also show that some of the features (excess argon, hydrous alteration) that pose obstacles to geochronology may nevertheless provide valuable information about the evolution of the rifting continental margin.

Before Gondwana breakup, the flood basalts of the Paraná-Etendeka Magmatic Province covered extensive areas in the southern portion of Brazil, eastern Paraguay, Uruguay, and northern Argentina in South America; and parts of Angola and Namibia in Africa (Piccirillo and Melfi, 1988; Peate, 1997; Thompson et al., 2001; Almeida et al., 2013; and references therein). Peak magmatism occurred at 134.7 ± 2 Ma (Renne et al., 1993, 1996; Thiede and Vasconcelos, 2010), but smaller magmatic events purportedly preceded and post-dated the main phase of extrusion (Mizusaki et al., 1992; Marques et al., 2018 and references therein; Gomes and Vasconcelos, 2021). Mafic dykes associated with the Paraná-Etendeka Magmatic Province are most abundant along the continental margins and areas from where the flood basalts have been eroded (Fig. 1). In South America, they cluster in the Ponta-Grossa (PGDS), Florianópolis (FDS), and Serra do Mar (SMDS) dyke swarms (Fig. 1), but associated intrusions occur further south in Uruguay (Cuaró dykes, Ures et al., 1997), and as far north as the Parnaíba Basin (Fig. 1) (e.g., Baksi and Archibald, 1997; Fernandes et al., 2020). In Africa, they occur in the Namibe Basin, Möwe Bay, Doros, South of Brandberg, Horingbaai, and Henjes Bay-Outjo dyke swarms (e.g. Thompson et al., 2001; Ewart et al., 1998).

At face-value, K-Ar and $^{40}Ar/^{39}Ar$ geochronology indicate that mafic dykes were emplaced before, during, and significantly after the main Paraná-Etendeka volcanic phase. The K-Ar results are dubious and suffer from some of the intrinsic limitations of the method (Vasconcelos et al., 2008), but many of the $^{40}Ar/^{39}Ar$ results are also ambiguous, show complex K and Ar systematics and suggest that some of the results may not reflect true ages of intrusion. For example, the Florianópolis dykes (Fig. 1) yield plagioclase single crystal incremental-heating ages of 129.4 ± 0.6 and 116.4 ± 7.8 Ma (Deckart et al., 1998) or 128.3 ± 0.8 to 119.0 ± 1.4 Ma (all age uncertainties at 1σ; Raposo et al., 1998), substantially younger than extrusive igneous rocks in the area. All age spectra are disturbed by excess argon, and most of the plateaus correspond to less than 50% of the ^{39}Ar released. In contrast, ID-TIMS U-Pb geochronology of three baddeleyite fractions yields a crystallization age of 134.7 ± 0.15 Ma (Florisbal et al., 2014), suggesting that at least some of the Florianópolis dykes are coeval with the main phase of Paraná flood basalt volcanism at ~134 Ma.

The Ponta Grossa dykes (Fig. 1) exhibit similar problems. $^{40}Ar/^{39}Ar$ laser incremental-heating analyses yield whole-rock plateau ages of 134.1 ± 2.6 to 130.4 ± 5.8 Ma (Turner et al., 1994). Turner et al. (1994) suggested that plagioclase alteration to clay minerals along fractures may have led to ^{40}Ar loss, lowering the measured ages. Renne et al. (1996) obtained young plateau ages, ranging from 131.4 ± 1.0 to 129.2 ± 1.0 Ma, for optically pristine plagioclase crystals from the Ponta Grossa dykes. Renne et al. (1996) reported two samples with even younger plagioclase plateau ages (125.8 ± 1.2 and 120.8 ± 1.4 Ma), interpreteded as minor intrusive activity related to the full drift stage and ocean basin formation.

$^{40}Ar/^{39}Ar$ geochronology for the Serra do Mar dykes (Fig. 1) is also problematic. Turner et al. (1994) obtained ages ranging from 135.8 ± 2.2 to 129.4 ± 1.2 Ma by laser incremental-heating analyses on whole-rock and plagioclase crystals from the central coast of the swarm. Deckart et al. (1998) reported plagioclase age spectra affected by excess argon and the presence of secondary phases; ages ranged from 134.5 ± 0.8 to 129.8 ± 0.4 Ma and were based on flat segments that represent less than 50% of the cumulative ^{39}Ar release, failing to define true plateaus (Fleck et al., 1977). Guedes et al. (2005) also obtained flat segments and plateau ages ranging from 146.8 ± 1.4 to 132.4 ± 0.6 Ma for plagioclase crystals and whole-rock grains from the central portion of the Serra do Mar dykes; all $^{40}Ar/^{39}Ar$ old results are affected by excess argon. Guedes et al. (2016) reported additional flat segments – not true plateaus – defining ages of 155.4 ± 1.7 and 149.8 ± 1.7 Ma for whole-rock analyses from the same swarm. Isochrons for the same grains confirm the presence of significant excess argon.

The Cabo Frio Tectonic Domain dykes (Schmitt et al., 2016), a northern component of the Serra do Mar dykes, also show significant amounts of excess argon, yielding saddle-shaped incremental-heating spectra. For example, Bennio et al. (2003) reported $^{40}Ar/^{39}Ar$ maximum ages of 77 ± 14, 54.8 ± 0.6 and 55.2 (uncertainty not provided) Ma for plagioclase crystals from tholeiitic dykes from Cabo Frio (Fig. 1). The pronounced saddled-shape spectra suggest large amounts of excess argon; the absence of statistically valid age plateaus or isochrons makes it impossible to evaluate the accuracy of these results.

More recently, Almeida et al. (2021) reported $^{40}Ar/^{39}Ar$ results for plagioclase crystals from four Cabo Frio Tectonic Domain dykes. The samples analyzed failed to provide reproducible results and flat segments do not yield plateaus as defined by Fleck et al. (1977); some are incorrectly identified as "integrated age". The reported magmatic ages (130.3 ± 11.0 and 120.6 ± 6.0 Ma) are averaged from results that range by as much as 30 Ma.

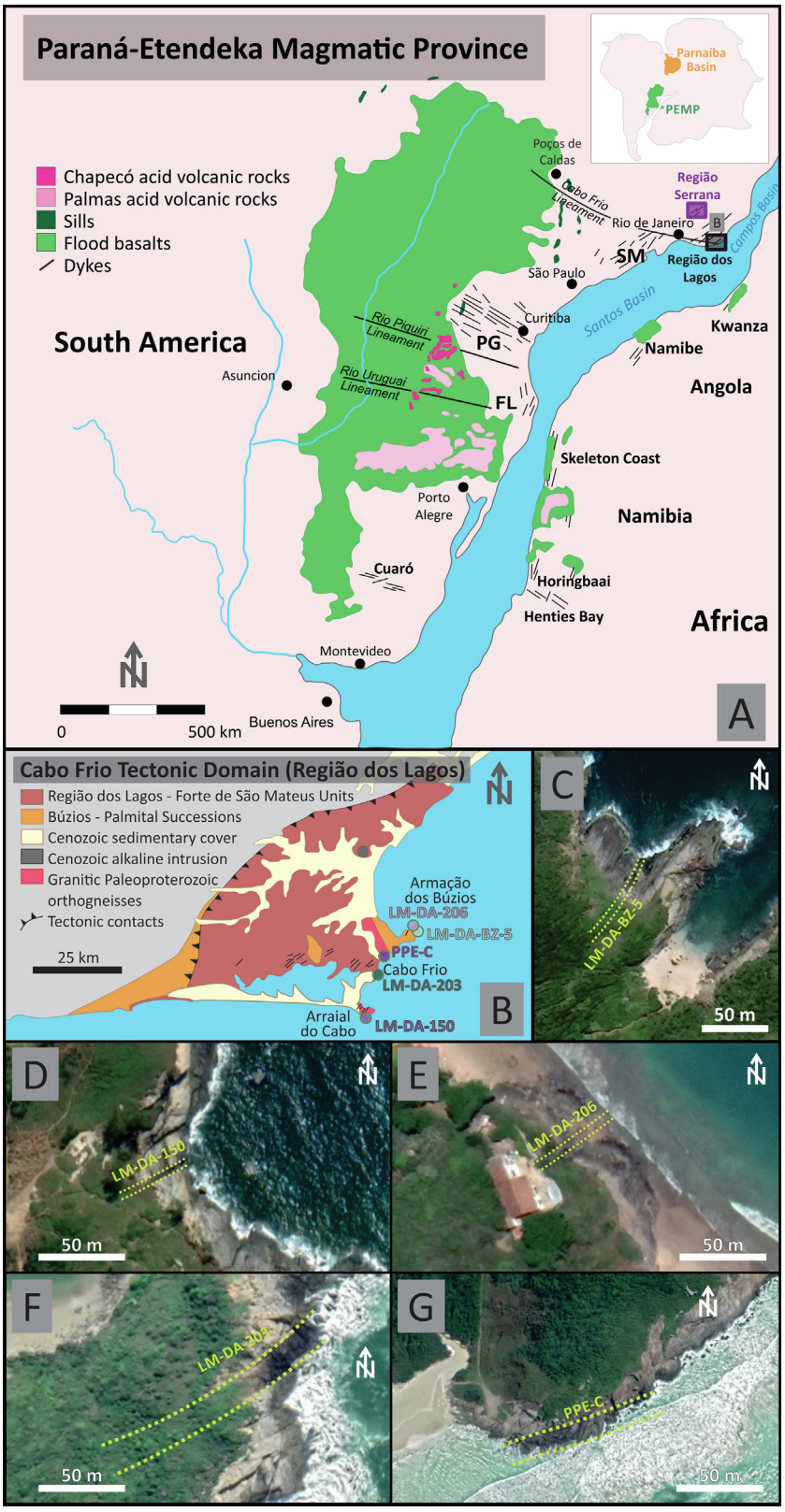

Fig. 1. A – Map of the Paraná-Etendeka Magmatic Province (PEMP) during early stages of South Atlantic expansion (Piccirillo and Melfi, 1988; Machado et al., 2015). SM: Serra do Mar dyke swarm. PG: Ponta Grossa dyke swarm. FL: Florianópolis dyke swarm. B – Cabo Frio Tectonic Domain, in Região dos Lagos (Schmitt et al., 2016), where all samples investigated here were collected. The four samples selected for $^{40}Ar/^{39}Ar$ geochronology and Sr, Nd and Pb isotope analyses are highlighted. C – Dyke LM-DA-BZ-5, from Armação dos Búzios. D – Dyke LM-DA-150, from Arraial do Cabo. E – Dyke LM-DA-206, from Armação dos Búzios. F – Dyke LM-DA-203, from Cabo Frio.

The wide range in the $^{40}Ar/^{39}Ar$ ages reported for Serra do Mar tholeiitic dykes (~155 to ~55 Ma) may indicate that mantle thermal anomalies and crustal extension started early in the history of Gondwana breakup, long before massive extrusion of continental flood basalts (Rocha-Júnior et al., 2013, 2020). The geochronological data may also suggest that intrusive magmatism was coeval with flood basalt volcanism and may have lasted for a long time after continental breakup because of persistent thermal anomalies and/or fault reactivation. Alternatively, the results may indicate that the $^{40}Ar/^{39}Ar$ system in some of these mafic dykes is complex and susceptible to excess argon and post-magmatic alteration, where the interpreted results may not reflect true ages of magma emplacement. Similar ambiguities are present in $^{40}Ar/^{39}Ar$ results for mafic dykes emplaced during Gondwana breakup in other regions of South America and Africa (e.g., Baksi and Archibald, 1997; Marzoli et al., 1999; Gomes and Vasconcelos, 2021). Unfortunately, confirming $^{40}Ar/^{39}Ar$ ages with U-Pb results, as done by Florisbal et al. (2014), is not always possible due to the absence of suitable minerals.

In order to devise an approach for properly dating mafic dykes by the $^{40}Ar/^{39}Ar$ laser-heating method, to identify and possibly overcome difficulties associated with alteration and excess argon, and possibly derive useful geological information from the altered dykes, we sampled and analyzed distinct phases from four Serra do Mar dykes, located within the Cabo Frio Tectonic Domain. These dykes are ideal targets because of the presence of both altered and unaltered K-bearing phases, and their previously measured saddle-shaped age spectra (Bennio et al., 2003) and variable ages (Almeida et al., 2021).

We also investigated the dykes for whole-rock major, minor, trace element, and isotopic geochemistry to determine potential fluid-rock interactions during dyke ascent, emplacement, and exhumation. In addition, major and trace element electron microprobe data and laser ICP-MS elemental mapping of single crystals of plagioclase helped to identify specific fluid-rock interactions recorded within the mineral. Identifying and possibly dating alteration events make it possible to investigate water-rock interaction as the crust extended due to rheological changes during and after supercontinent breakup.

2. GEOLOGICAL CONTEXT

2.1. Regional tectonics

All dykes investigated here were emplaced in the Região dos Lagos, within the Cabo Frio Tectonic Domain (CFTD; Fig. 1), a block that collided with the Ribeira belt during the Búzios Orogeny (520 to 510 Ma) and was later fragmented by Cretaceous rifting (Schmitt et al., 2016; and references therein).

The CFTD Paleoproterozoic basement rocks record low-angle deformation and low- to medium-pressure metamorphism and comprise two main groups: felsic metagranitoids, diorites and migmatitic gneisses from the Região dos Lagos Unit; and amphibolitic banded gneisses from the Forte de São Mateus Unit (~1970 Ma protoliths; ~520 Ma metamorphism; Schmitt et al., 2004). The Búzios and Palmital Units, which also host some of the dykes investigated in this study, are amphibolitic, calcium-silicate and quartz-feldspar meta-igneous and -sedimentary complexes that represent ocean floor deformed during the Búzios Orogeny (~500 Ma; Schmitt et al., 2004, 2016; and references therein).

The collision, subduction and extension events that affected the CFTD have probably decreased its crustal strength and thickness; in fact, receiver function seismology indicates a shallow Moho discontinuity (~38 km; Assumpção et al., 2002; Schmitt et al., 2016). Additionally, NE-SW-oriented magnetic and gravimetric anomalies following basement structural trends can be traced from the CFTD onshore to the Santos Basin offshore, suggesting that intrusive magmatism was more intense bellow the thinned crust and extended into marginal basins (Oreiro et al., 2008; Stanton et al., 2010). Extensional tectonism resulted from simultaneous fault reactivation and magma ascent, a combination that potentially minimized the stresses required for continental breakup (Lavecchia et al., 2016).

2.2. The Cabo Frio Tectonic Domain dykes within the Serra do Mar Dyke Swarm

The Serra do Mar dyke swarm extends along São Paulo and Rio de Janeiro, southeastern Brazil (Fig. 1), and it comprises vertical/sub-vertical NE-SW dykes that follow basement structural trends (Corval et al., 2008). The dykes are either high- (HTi: $TiO_2 > 2$ wt%) and low-Ti (LTi: $TiO_2 < 2$ wt%) tholeiites, sharing similarities with HTi Pitanga-Urubici and LTi Esmeralda-Gramado basalts from the Paraná-Etendeka Magmatic Province (e.g., Bellieni et al., 1990; Peate et al., 1992). The LTi dykes represent only ~10% of the swarm and occur in the Região dos Lagos, in the CFTD, and in the Região Serrana of Rio de Janeiro, within the Serra do Mar mountains (Fig. 1; e.g., Corval et al., 2008).

According to Bennio et al. (2003), the dykes in the CFTD are subalkaline, with trace element and Sr isotopic signatures that preclude significant crustal assimilation, and comprise two distinct magmatic suites: group A, more primitive ($SiO_2 < 52$ wt%; MgO > 5.5 wt%; $145 \leq [Sr] \leq 229$ ppm; $66 \leq [Zr] \leq 114$ ppm; $0.70426 \leq {}^{87}Sr/{}^{86}Sr_i \leq 0.70434$ and $0.51659 \leq {}^{143}Nd/{}^{144}Nd_i \leq 0.51267$); and group B, more evolved ($SiO_2 > 52$ wt%; MgO < 6 wt%; $227 \leq [Sr] \leq 264$ ppm; $93 \leq [Zr] \leq 154$ ppm $0.70548 \leq {}^{87}Sr/{}^{86}Sr_i \leq 0.70613$ and $-0.51238 \leq {}^{143}Nd/{}^{144}Nd_i \leq 0.51239$). Simple mixing, assimilation, and fractional crystallization models do not show petrogenetic relationships between the two suites (Bennio et al., 2003).

Precise emplacement ages of the CFTD dykes are relevant to understand continental rifting as their SW-NE direction is parallel to the continental margin, which suggests a close relationship with rift faulting. Their location also coincides with the coastal extension of the Cabo Frio Lineament, a 500 km-long WNW-ESE series of 85 to 50 Ma syenitic-carbonatitic plutons and alkaline dykes

between Poços de Caldas, Minas Gerais, and Cabo Frio, Rio de Janeiro (Fig. 1). According to Ferroni et al. (2017), this magmatic series marks the reactivation of a deep lithospheric fracture zone during seafloor spreading. Magmatic activity along this trend continued into the offshore basins, comprising the Alto do Cabo Frio magmatism (Stanton et al., 2010; Oreiro et al., 2008).

3. SAMPLING AND ANALYTICAL PROTOCOLS

Twelve tholeiitic dykes (Table 1) were sampled at Arraial do Cabo, Cabo Frio and Armação dos Búzios (Fig. 1B), within the CFTD. The dykes range from small aphanitic bodies (tens of cm wide) to large (up to 20 m wide) intrusions that are holocrystalline and equigranular in the center, and aphanitic at the chilled margins. Samples were collected from non-weathered and xenolith-free central zones of > 3 m dykes, except for dyke PPE-C, sampled both at the margin (PPE-C1) and the center (PPE-C3). Most of the intrusions trend N40°E-N70°E (Fig. 1).

All dykes are visually free from weathering (no dissolution cavities, no iron oxyhydroxide staining, no visible clay minerals, etc.). However, they exhibit both sericitized (milky white) and apparently pristine (clear and transparent) plagioclase phenocrysts (500–1000 μm). One of them (LM-DA-203) also contained considerable amounts of amphibole and biotite (~5% of the assemblage). Four of the dykes – LM-DA-BZ-5, LM-DA-203, LM-DA-150 (highlighted in Table 1), and PPE-C – were dated by $^{40}Ar/^{39}Ar$ geochronology. Eleven of the dykes were investigated by a comprehensive set of additional analytical methods: optical microscopy for general petrographic characterization; scanning electron microscopy (SEM) and electron probe microanalysis (EPMA) for mineral identification and composition; X-ray fluorescence (XRF) for whole-rock major and minor element composition; inductively coupled plasma mass spectrometry (ICP-MS) for whole-rock trace element composition; and thermal ionization mass spectrometry (TIMS) for Sr and Nd isotopic composition. Because of its phenocryst assemblage (clear plagioclase, milky plagioclase, clinopyroxene, olivine, amphibole, biotite, and magnetite phenocrysts), dyke LM-DA-203 was targeted for detailed geochronology and mineral-specific trace-element mapping by laser ablation ICP-MS (LA-ICP-MS).

3.1. $^{40}Ar/^{39}Ar$ Geochronology

Basic mineral characterization, including the identification of alteration phases, preceded geochronological analysis; it included transmitted- and reflected-light optical microscopy (Nikon Eclipse E400 POL) and electron microscopy/EDS analysis (Hitachi Tabletop Scanning Electron Microscope TM3030 equipped with a Bruker Energy Dispersive Spectroscopy detector) on polished thin sections from four selected samples. Mineral separation was carried out at the Institute of Astronomy, Geophysics and Atmospheric Sciences and the Institute of Geosciences, University of São Paulo, Brazil, and at the University of Queensland Argon Geochronology in Earth Sciences (UQ-AGES) laboratory.

After removing weathered surfaces with an alumina grindstone (Al_2O_3), we crushed the samples selected for $^{40}Ar/^{39}Ar$ analyses to 80–150 mesh using a jaw crusher and a stainless-steel mortar-and-pestle. Magnetic and density mineral separation was carried out with hand magnets,

Table 1
Location, coordinates, thickness, and analytical methods used in the investigation of each of the 12 CFTD dyke samples.

Sample	Locality	Latitude	Longitude	Thickness (m)	Analytical methods
LM-DA-BZ-4	Armação dos Búzios	S22° 45′17.8″	W41° 51′54.8″	0.8	XRF; ICP-MS
LM-DA-BZ-5	Armação dos Búzios	S22° 45′17.8″	W41° 51′54.8″	3	XRF; ICP-MS; Sr, Nd, Pb isotopes, $^{40}Ar/^{39}Ar$ geochronology
LM-DA-150	Cabo Frio	S22° 56′46.6″	W42° 01′42.3″	2.5	XRF; ICP-MS; Sr, Nd, Pb isotopes; $^{40}Ar/^{39}Ar$ geochronology
LM-DA-158	Arraial do Cabo	S22° 57′31.2″	W41° 01′34.7″	1.5	XRF; ICP-MS
LM-DA-182	Armação dos Búzios	S22° 59′25.5″	W42° 00′51.5″	-	XRF; ICP-MS
LM-DA-203	Cabo Frio	S22° 52′17.9″	W41° 58′47.2″	20	XRF; ICP-MS; Sr, Nd, Pb isotopes; $^{40}Ar/^{39}Ar$ geochronology
LM-DA-204	Cabo Frio	S22° 52′16.2″	W41° 58′59.0″	3	XRF; ICP-MS
LM-DA-205	Armação dos Búzios	S22° 46′10.0″	W41° 52′37.1″	2.5	XRF; ICP-MS
LM-DA-206	Armação dos Búzios	S22° 45′11.2″	W41° 52′26.4″	1	XRF; ICP-MS; Sr, Nd, Pb isotopes
LM-DA-208	Armação dos Búzios	S22° 45′06.6″	W41° 53′47.6″	1.5	XRF; ICP-MS
LM-DA-210	Armação dos Búzios	S22° 59′36.6″	W42° 00′51.5″	2.5	XRF
PPE-C	Cabo Frio	S22° 49′22.1″	W41°58′8.2″	20	$^{40}Ar/^{39}Ar$

a Frantz separator, and bromoform (2.81 g/cm^3). For sample LM-DA-BZ-5, 0.2–2 mm sericite-free (clear) and sericitized (milky white) plagioclase crystals and visually unaltered whole-rock fragments were handpicked. For sample PPE, sericitized (milky white) plagioclase crystals and whole-rock fragments were handpicked. For samples LM-DA-150 and LM-DA-203, 5–8 mg of 80–150 mesh sericite-free (clear) and sericitized (milky white) plagioclase crystals were handpicked and vacuum-encapsulated in 1 mm ID and 2-mm OD Si capillaries. Pristine amphibole and biotite aggregated grains from sample LM-DA-203, ranging from 100 to 150 μm, were also hand-picked and encapsulated in Si capillaries. Capsules were pumped for eight hours to 10^{-8} Torr and sealed with a methane-O_2 torch, following the procedures of Ren and Vasconcelos (2019). Vacuum-encapsulation helped to test whether the fine-grained samples were susceptible to significant ^{39}Ar recoil losses.

Single crystals and rock fragments were inserted into individual wells in high-purity Al irradiation disks together with Fish Canyon sanidine fluence monitors (accepted age of 28.201 ± 0.046 Ma; Kuiper et al., 2008) and GA1550 biotite as a secondary standard (98.8 ± 0.5 Ma; Renne et al., 1998), following the geometry illustrated in Vasconcelos et al. (2002). The encapsulated samples were inserted into hollow wells in a stack of five aluminum disks, where the lowermost disk was not hollow and held Fish Canyon monitors at the bottom of the wells, in the same horizontal level as the grains in the capsules, as illustrated in Ren and Vasconcelos (2019). The disks were wrapped in Al-foil, sealed into a silica capsule containing up to 11 Al disks, and irradiated for 14 hours in the Cd-lined B-1 CLICIT facility at the Oregon State University TRIGA reactor, USA.

After irradiation, noble gas mass spectrometry was performed in a fully automated MAP-215–50 mass spectrometer equipped with a Balzers 217 electron multiplier at UQ-AGES. The individual crystals of GA1550 biotite were irradiated in the same disks as our samples and were analyzed separately. They yielded flat spectra and reproducible plateau, isochron, and kernel density probability ages (Table 2; plots are available in supplementary material A). All results are indistinguishable from the proposed values for this international standard (Renne et al., 1998; Spell and McDougall, 2003), attesting to the reliability of the procedures.

The capsules containing plagioclases from samples LM-DA-203 and LM-DA-150 were drilled with a Lambda-physik MINex Excimer KrF laser so that any possible ^{39}Ar dislodged from the crystals by recoil or heating during irradiation could be analyzed prior to the step-heating procedure. Once the capsules had been pierced and the first step from each capsule had been analyzed, the same sample chamber containing the copper disks with the capsules was placed under a Coherent Verdi 10 W diode laser, where the grains were incrementally heated by a 2-mm wide laser beam programmed to progressively travel along the Si-capsules containing the grains. Single crystals and whole-rock fragments from samples LM-DA-BZ-5 and PPE-C were also incrementally heated with a Coherent Verdi 10 W diode laser with a similar 2-mm beam.

The fractions of gas released by piercing or incremental heating passed through a cryocooling device operated at −130 °C (H_2O and CO_2 removal) and two SAES C-50 getter pumps, the first at ~475 °C and the second at room temperature. The gas was then expanded into the mass spectrometer, equipped with a third SAES C-50 getter pump. One sequence of three blanks and one air-pipette shot (in the order blank-air-blank-blank) was analyzed before and after each sample to monitor background values and to quantify Ar isotope discrimination (assuming the atmospheric ^{40}Ar/^{36}Ar value of 298.56 ± 0.31 of Lee et al., 2006).

J-factors for each Al-disk were calculated from the laser total-fusion analyses of 15 individual aliquots (1–3 individual grains) of Fish Canyon sanidine grains. Irradiation parameters, Ar isotope discrimination, atmospheric gas contributions, and blanks and baseline corrections were calculated using the Mass Spec software (Deino, 2012). The ages and associated uncertainties were determined by propagating measured Ar isotope values to time zero with either linear or parabolic regressions, subtracting the values for blanks and baselines, and correcting for discrimination and errors in the J parameter and irradiation parameters. The results for discrete analysis from each grain were plotted in % cumulative ^{39}Ar released *versus* apparent age spectra, and age plateaus were defined as at least three consecutive steps yielding apparent ages within 2σ error from the variance-weighted mean, comprising 50% or more of total ^{39}Ar released (Fleck et al., 1977).

3.2. Major, minor and trace element whole-rock analyses

In order to evaluate geochemical characteristics and possible alteration effects on the chemistry of the different

Table 2
GA1550 results.

Sample	Plateau			Isochron			Probability density plot		
	Age	MSWD	Steps	Age	MSWD	Steps	Intercept	Mean weighed age	MSWD
9240-01	98.83 ± 0.32	1.67	10	98.70 ± 0.35	1.6	16	295.2 ± 7.8	98.70 ± 0.14	1.55
9240-02	98.55 ± 0.36	1.63	10						
7474-01	98.49 ± 0.41	0.7	9	98.50 ± 0.37	0.89	19	296.0 ± 17	98.49 ± 0.18	0.85
7474-02	98.49 ± 0.50	1.13	10						
7495-01	99.15 ± 0.63	1.42	9	98.87 ± 0.58	1.4	19	292.0 ± 34	98.63 ± 0.27	1.04
7495-02	98.36 ± 0.65	0.52	10						
7516-01	98.85 ± 0.61	1.05	10	98.65 ± 0.54	1	19	291.0 ± 14	98.82 ± 0.50	0
7516-02	98.44 ± 0.59	0.82	9						

dykes, we prepared whole rock fractions of 11 dykes for major, minor, and trace element, and Sr, Nd and Pb isotope analyses at the Institute of Astronomy, Geophysics and Atmospheric Sciences, University of São Paulo. Samples were crushed in fragments of less than 0.5 cm diameter using a hydraulic press and a stainless-steel jaw crusher with the same procedures described in Marques et al. (2016). After quartering, samples were washed with double distilled water, ultrasonicated in purified 0.1 M HNO_3 and deionized water, and later dried inside clean boxes in a class 10,000 clean room (Marques et al., 1999, 2016). The fragments were then pulverized using an agate mill (Marques et al., 2016).

Major and minor oxide analyses were performed at the XRF Laboratory of the Universidade Estadual Paulista (UNESP-Rio Claro), following procedures described by Nardy et al. (1997) and Machado et al. (2015). Reference basalts BHVO-2 and BE-N were analyzed as primary standards with major and minor element accuracies better than 7%, with typical values ranging between 1 and 3% (supplementary material B).

Rare earth and other trace elements (Cr, Ni, Ba, Rb, Sr, Zr, Y, Nb, Ta, Th, U, Pb, Hf, Sc, Co) were analysed with ICP-MS at the Geochemistry Laboratory, Universidade Estadual de Campinas. Replicate analyses of the BRP-1 reference material (a basalt rock from the Northern portion of the Paraná-Etendeka Province; Cotta and Enzweiler, 2008) showed that the accuracy was better than 10% for most of the elements; Rb (26%) and Cr (46%) are exceptions (supplementary material C).

Four representative samples were analysed for Sr and Nd isotope compositions by thermal ionization mass spectrometry at the Institute of Geosciences, University of São Paulo. The rock powders (100 mg) were dissolved in Savillex beakers with HF and HNO_3 on a hot plate for 5 days at ~110 °C and were dried down on a hot plate; the residue was dissolved in 6 M HCl at 110 °C for 24 hours. The HCl solution was dried down and concentrated HNO_3 was added on the residues. Samples were taken to dryness prior to re-dissolution for ion exchange purification.

Sr was purified using Eichrom Sr-Spec® resin and eluted with 0.05 M HNO_3. A Triton TIMS (thermal ionization mass spectrometer) in dynamic mode was used for Sr isotope analysis (normalization ratio $^{86}Sr/^{88}Sr = 0.1194$ and analytical blank values of 119 pg), with an accuracy of 0.015% for NBS-987 standard ($^{87}Sr/^{86}Sr = 0.710237 \pm 0.000024$, total of 33 analyses from May/2015 to March/2016. Samples were analysed in March/2016).

Nd was purified using two sets of ion-exchange columns with RE-Spec® and LN-Spec®; Nd was eluted in 0.26 M HCl. Isotope ratios were measured in a Thermo Neptune ICP-MS (normalization ratio $^{146}Nd/^{144}Nd = 0.7219$ and blank values were below 40 pg) with an accuracy of 0.0012% for the JNdi-1 standard ($^{143}Nd/^{144}Nd = 0.512086 \pm 0.000006$, n = 20).

3.3. Chemical characteristics of plagioclase and secondary phases

Altered plagioclase crystals were initially characterized on polished thin sections by electron microscopy (Hitachi SU3500 Scanning Electron Microscope equipped with an Energy Dispersive Spectroscopy system; SEM-EDS) in the Centre for Microscopy and Microanalysis (CMM), University of Queensland. Major element compositions were measured by Electron Probe Microanalysis (EPMA) with a JEOL JXA-8200 Wavelength Dispersive X-ray Spectrometer (WDS) and EDS instrument at CMM-UQ. Thin sections were carbon-coated and analyzed under high-vacuum at an accelerating voltage of 15 kV, a 2 μm diameter electron beam, 15nA beam current, and counting times of 10 s on peak and 5 s on each of two background positions.

The WDS system was calibrated using the following Micro-Analysis Consultants crystals: albite-t-ox (Al-TAP, Na-TAP), P140-olivine (Mg-TAP), wollastonite-t (Si-TAP, Ca-PETJ), orthoclase-1 (K-PETJ), spessartine-ox (Mn-LIF), chromite-t-ox (Fe-LIF, Cr-PETJ), Ni-olivine-G (Ni-LIF), apatite-t (P-PETJ), rutile-ox (Ti-PETJ); all in Kα position. Matrix effects were corrected using the ZAF procedure (Z – atomic number; A – absorption; F – fluorescence). The international reference materials Kakanui hornblende, Kakanui augite, Lake Co feldspar, VG2 basaltic glass and Springwater olivine were used to monitor the accuracy of analyses of unknowns. Accuracy was typically better than 1–5%, except for elements with abundances below 1%, for which accuracy was better than 20%. Plagioclase phenocrysts were analyzed along transects. All oxide results with analytical totals between 98–102% were then manually corrected with the calibration factors obtained for the standards. The final data was screened through stoichiometry tests for calcic plagioclase; the final dataset comprises 228 major element analyses (supplementary material D).

Major, minor and trace element maps (Ca, Si, Fe, K, Na, Ba, Li, Rb, Sr, Pb, U, La, Ce, Nd, Sm, Yb) were generated by LA-ICP-MS at the University of Queensland Centre for Geoanalytical Mass Spectrometry, Radiogenic Isotope Facility (UQ RIF Lab), following the methodology developed by Ubide et al. (2015, 2019). Thin sections were loaded in a dual-volume Laurin Technic ablation cell controlled by GeoStar Norris software. We ablated the plagioclase crystals and surrounding groundmass using an ASI RESOlution 193 nm excimer UV ArF laser system and progressively moved the sample stage under the fixed laser beam to produce uniform ablated lines with overlapping squares (3 J/cm^2 fluence, 10 × 10 μm square mask, 10 μm/s translation speed, 10 Hz repetition rate, 1 μm overlap between rasters). Pre-ablation was performed with a 100 × 100 μm laser aperture, 200 μm/s speed and 20 Hz to enhance laser-crystal coupling. Ablation took place in an ultrapure He environment (350 mL/min flow), and Ar (850–950 mL/min) and N_2 (5 mL/min) flows in the plasm torch promoted efficient ionization and transport.

Elemental data were measured in a Thermo iCap RQ quadrupole mass spectrometer, and instrument calibration used the NIST612 glass reference material. Elemental maps were processed with Iolite v.2.5 (Paton et al., 2011) in quantitative mode. NIST612 was used as calibration standard, and the EPMA average calcium concentration in plagioclase phenocrysts (15.99 ± 1.48 wt% CaO) was used as

internal standard because of the low CaO variation in comparison with other major elements (including SiO_2). For this reason, the results are quantitative for plagioclase crystals, and semi-quantitative for other phases. Accuracy and precision were calculated using BHVO-2G and BCR-2G glasses as secondary standards. Precision was better than 5% and accuracy was better than 5–10% for all trace elements. We also measured K and Fe to track relative variations in the mapped areas; results from these elements were treated as semi-quantitative.

We used the Monocle add-on for Iolite (Petrus et al., 2017) to estimate the compositions of selected crystal zones (supplementary material E). We based the selections on Ca and Fe zoning and defined polygons of homogeneous composition (i.e., where standard deviations were lowest). This approach returned compositions of high precision relative to spot analyses.

4. RESULTS

4.1. Petrography of samples investigated by $^{40}Ar/^{39}Ar$ geochronology

The dykes are holocrystalline and ophitic and have olivine diabase composition (Le Maitre et al., 2002), comprising mostly plagioclase, pyroxene, magnetite, ilmenite, olivine, biotite and amphibole. Most intrusions are porphyritic, with plagioclase, pyroxene and minor olivine, amphibole or biotite phenocrysts in a microcrystalline matrix of plagioclase, pyroxene and magnetite microlites. The central portions of wide dykes (>5 m wide) are equigranular. Partially altered rocks contain chlorite, pyrite, chalcopyrite and sericite. Chloritization is significant in one of the dykes (LM-DA-210), and sericitization occurs in most of them, mainly in plagioclase bytownitic cores, which are cloudy. Labradoritic compositions occur in phenocrysts rims and microlites, and rarely display any sericitization. The intensity of sericitization varies between dykes.

Selected images of the samples analyzed by $^{40}Ar/^{39}Ar$ geochronology are available in Fig. 2. Dyke LM-DA-203 is porphyritic along the borders and equigranular in the center, it is incipiently altered, and it contains plagioclase crystals with few fractures and magnetite, pyroxene, pyrite and apatite inclusions (Fig. 2C, D). Partial sericitization, if present, occurs in plagioclase cores and it results in lower average mineral density, as shown by the darker gray tones in backscattered images (Fig. 2A, B). Sericite is often associated to exceedingly small quartz crystals and albitized zones. Most of the fractures are filled with Fe and Mg-rich phases.

Some clear plagioclase phenocrysts show irregular rims marked by Na-enrichment and Ca-depletion that define albitized zones (6–11 wt% Na_2O, against 1–5 wt.% in sectors without enrichment), only noticeable in backscatter electron images, EDS analyses and LA-ICP-MS elemental maps (Section 4.2). Narrow Na-rich zones also occur in central regions of the crystals, next to fractures (Fig. 2D). Plagioclase microlites in the matrix are not altered.

Similar petrographic features are present in the other three samples. Dyke LM-DA-BZ-5 is porphyritic, and its plagioclase phenocrysts are either unaltered or pervasively sericitized in the core. They host magnetite, pyroxene, and pyrite inclusions. Irregular Na-rich zones are detectable by SEM/EDS analysis in many of the plagioclase phenocrysts (supplementary material K). The plagioclase microlites are unaltered.

Sample LM-DA-150 is porphyritic, with plagioclase phenocrysts showing pervasive core replacement by sericite and hosting apatite and sulfide inclusions (supplementary material K). They also show irregularly albitized zones. Sulfide crystals occur in the microcrystalline matrix, and no alteration is detectable in plagioclase microlites.

Lastly, dyke PPE-C is porphyritic at the border (PPE-C1; glass matrix) and equigranular with occasional plagioclase aggregates in the center (PPE-C3) (supplementary material K). In both PPE-C1 and PPE-C3, plagioclase phenocrysts and microlites are highly fractured, pervasively sericitized and display numerous apatite and sulfide inclusions. Na-enrichment in crystal rims and cores produce an irregular zonation pattern.

Additional petrographic images of plagioclase crystals from each of the dated samples are provided in supplementary material L.

4.2. Laser Ablation ICP-MS Mapping

LA-ICP-MS maps of Ca, Si, Fe, K, Na, Ba, Li, Rb, Sr, Pb, U, Sm, Nd, La and Yb concentrations for two representative altered plagioclase crystals from sample LM-DA-203 are shown in Figs. 3 and 4. Additional Ce maps are available on supplementary material F. Crystal I (Fig. 3) is embedded in a fine groundmass and its primary composition ranges from bytownite (core) to labradorite (rims). Sericite occurs in the core and in the vicinity of minor fractures. Major, minor and trace element maps show evidence for sericitization. The maps also show that LREEs (La, Ce etc.) were more affected by fluid percolation than HREEs (e.g., Yb). In crystal II (Fig. 4), primarily labradorite, albitization occurs as irregular rims and along fractures.

Independently of whether the crystal is sericitized or albitized, alteration is marked by an increase in Na, K, Si, and Fe and a decrease in Ca. Some fractures are filled with Si, Fe, Na and K-rich phases, but alteration penetrates beyond the fractures into the crystals and reveal solution-feldspar cation exchange (especially noticeable in Ca and Na maps, Fig. 4). The LA-ICP-MS analyses also show that sericitization is accompanied by Ba, Li, Rb, Sr, Pb, Na, and, to a lesser extent, Sm, Nd and La enrichment; albitization also shows Ba, K, Li, Sr and Pb enrichment. Li and Pb are particularly enriched along fractures.

Elemental enrichment in the alteration zones and fractures in crystals I and II (Figs. 3 and 4, respectively) is quantitatively evaluated in Fig. 5, in which average elemental concentrations were extracted from altered zones and normalized by the calcic plagioclase average values. The average values, ratios and figures of the selected regions are available in supplementary material E. Sm, Yb and U were excluded from the plots due to their high average uncertainties, which result from the low and scattered signals within the alteration zones and fractures.

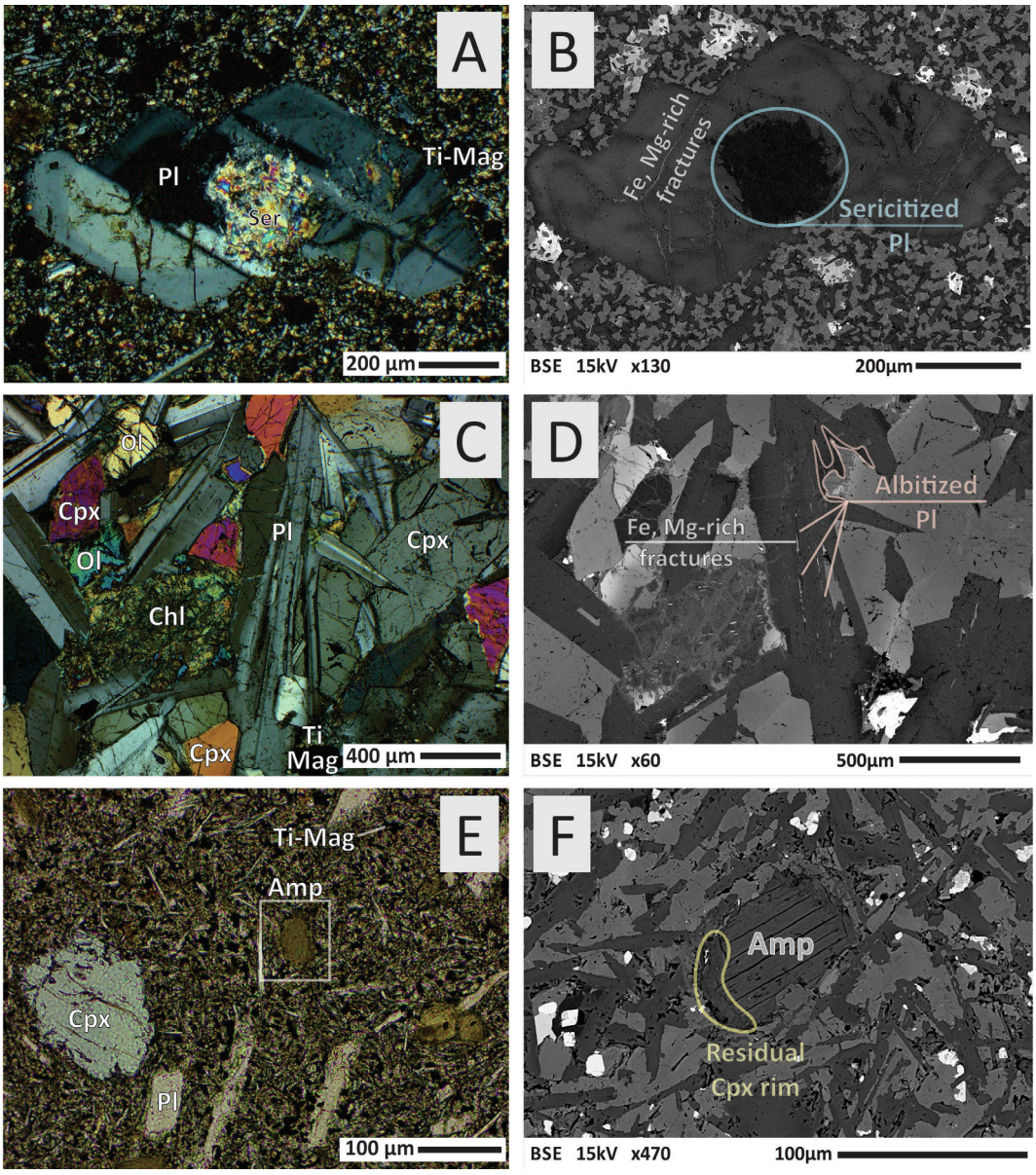

Fig. 2. A – Cross-polarized photomicrograph of a sericitized (Ser) plagioclase phenocryst (Pl) from the border region of the dyke where LM-DA-203 was collected, along with magnetite (Ti-Mag) in a fine-grained matrix. B – Backscattered image of A. C - Cross polarized photomicrography of a clear partially albitized plagioclase phenocryst (Pl) in sample LM-DA-203 (center of the dyke), along with titanomagnetite (Ti-Mag), clinopyroxene (Cpx) and partially chloritized (Chl) olivine (Ol). D – Backscattered image of C. Albitization zones occur randomly in borders and along fractures; some of them are highlighted. E - Cross-polarized photomicrograph of an amphibole (Amp) crystal close to the border of the same dyke. Plagioclase, clinopyroxene and titanomagnetite phenocrysts are also shown. F - Backscattered image of the boxed region in E. A residual rim of the original clinopyroxene is highlighted.

The sericitized core in crystal I (Fig. 5) is enriched in all analyzed elements when compared to the pristine plagioclase. Rb, Ba, K and Li are particularly enriched in sericitized zones. Albitized zones in crystal II are also enriched in all elements when compared to the pristine crystal, but to a lesser degree.

4.3. Geochronological results

Four grains from sample LM-DA-BZ-5 were analyzed by the laser incremental-heating method: one whole-rock fragment (Lab #9237); one clear plagioclase crystal (Lab #9238); and two cloudy and sericitized plagioclase crystals (Lab #9239-01 and -02) (Fig. 6). All four samples yielded saddle-shaped spectra. The whole-rock chip (Lab #9237) yielded the most pronounced saddle-shape spectrum, with apparent ages at 168.0 ± 8.2 Ma (Fig. 6A) and unreasonably old apparent ages in the initial and final steps. The clear plagioclase crystal (Lab #9238) shows a saddle-shaped spectrum with a trough defining an apparent age estimate of 138.6 ± 2.5 Ma (Fig. 6B). These results can be interpreted as maximum ages of intrusion, but it is

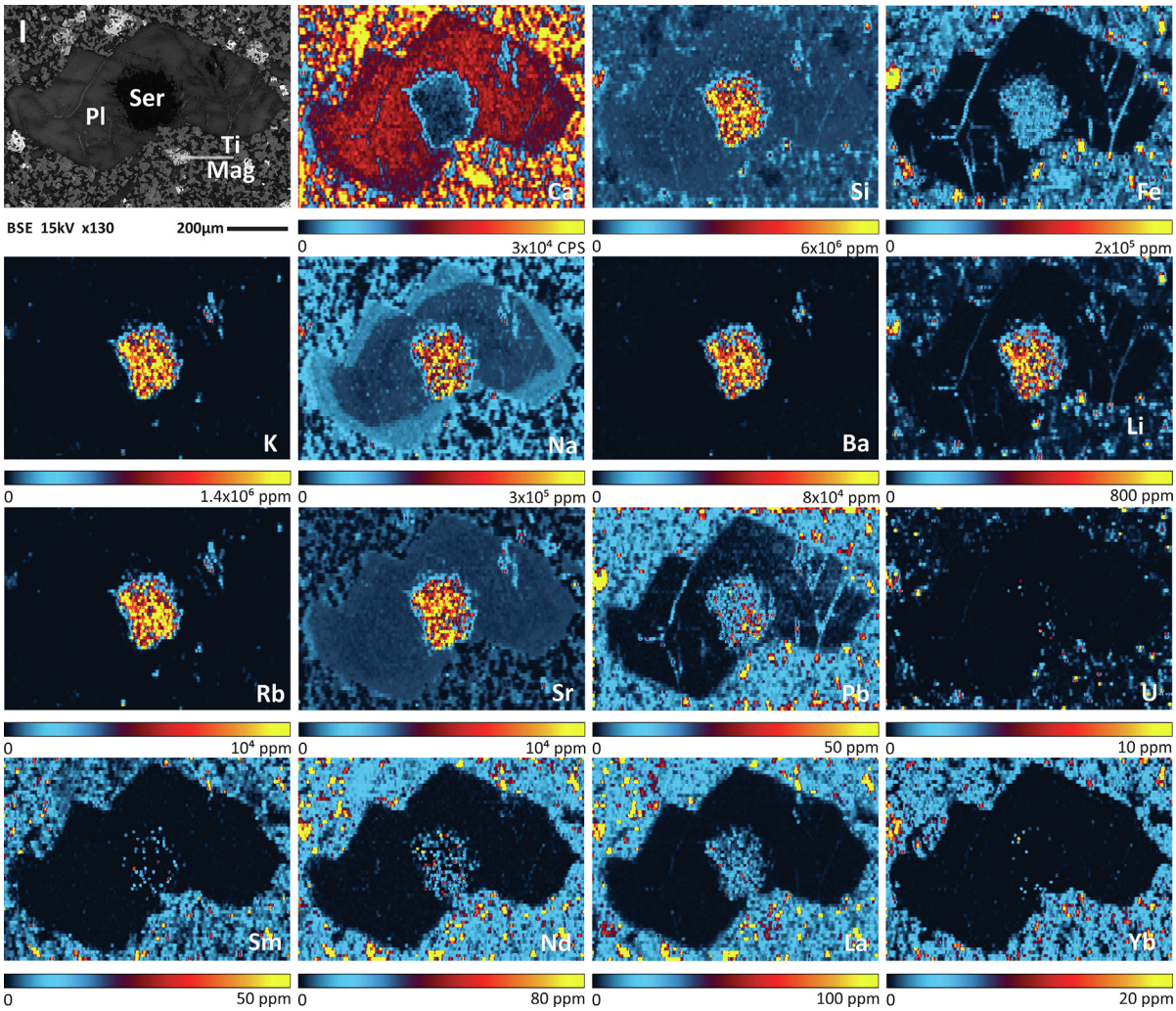

Fig. 3. Backscattered electron images and LA-ICP-MS elemental maps of the sericitized plagioclase crystal I (also shown in Fig. 2A, B) from sample LM-DA-203, collected at the border of the dyke, where the texture is porphyritic. Colour scales reflect concentration values in plagioclase (parts per million), except for the Ca map, which represents signal intensity (counts per second; internal standard). Analyses are quantitative for plagioclase and semi-quantitative for other phases in the groundmass.

impossible to make further inferences. The two cloudy and sericitized plagioclase crystals yielded similar but not exactly reproducible saddle-shaped spectra that suggest variable amounts of excess argon in both grains (Fig. 6C). The trough defined by the intermediate-temperature steps reached flat segments with distinct apparent age estimates of 131.9 ± 4.8 Ma and 124.1 ± 2.5 Ma that are also difficult to interpret.

Whole-rock fragments (Lab #7456-01 and -02 and #7457-01 and -02) and two plagioclase crystals (Lab #7459-01 and -02) from sample PPE-C also display saddle-shape spectra with no plateaus. Whole-rock chips from the center of the dyke (Lab #7457-01 and -02) yielded spectra with intermediate temperature apparent ages at 168.0 ± 12.0 and 167.6 ± 4.0 Ma (Fig. 6D); whole-rock chips from the dyke border (Lab #7456-01 and −02) yielded spectra with apparent ages at 137.8 ± 1.5 Ma and 137.2 ± 1.6 Ma (Fig. 6E). The only useful information retrievable from these results is that they identify maximum ages of intrusions, not particularly informative given the large scatter. Two sericitized plagioclase crystals from sample PPE-C (Lab #7457-01 and -02) yielded flat segments (no plateaus) that define apparent ages of 111.5 ± 1.2 Ma and 109.6 ± 5.5 Ma (Fig. 6F), showing that sericitization lowered the apparent ages and simultaneously masked the effects of excess argon components. The combination of excess argon (which increases the apparent age) with the presence of alteration phases (which lowers the apparent age) in a same grain or sample makes it impossible to retrieve much useful geochronological information from the results, other than the fact that the lowest apparent ages obtained record the maximum age of alteration.

Given the persistent presence of excess argon in whole-rock grains, we focused on dating selected mineral aliquots in samples LM-DA-203 and LM-DA-150. Since some of the pure mineral fractions were very fine grained, we dated

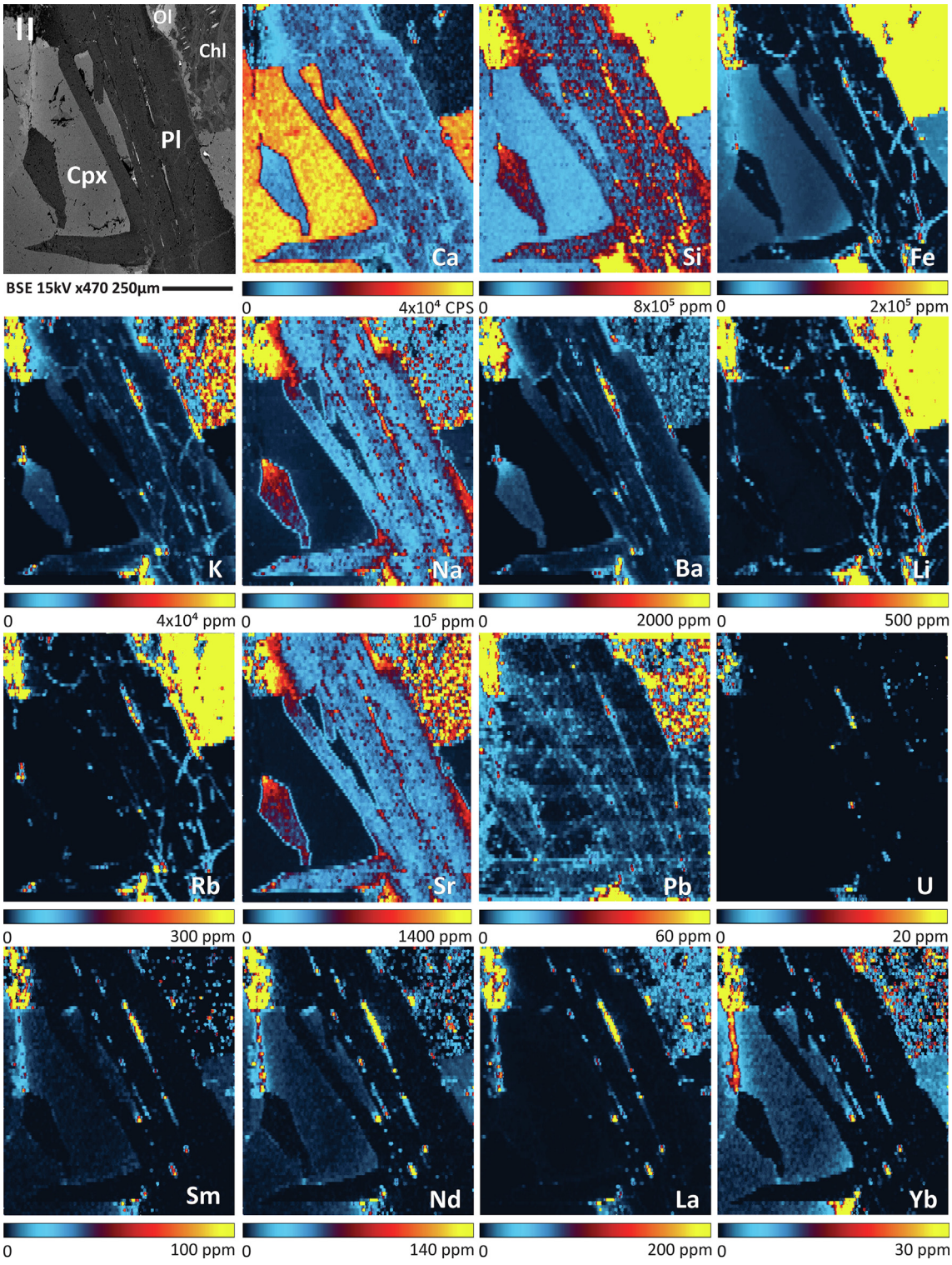

Fig. 4. Backscattered electron images and LA-ICP-MS elemental maps of the albitized plagioclase crystal II (also shown in Fig. 2C, D) from sample LM-DA-203. Plagioclase is bordered by olivine, chlorite, and clinopyroxene. Colour scales reflect concentration values in parts per million, except for the Ca map which represents signal intensity (counts per second; internal standard).

the small crystals as silica-encapsulated aliquots both for ease of manipulation but also to measure and obviate any possible ^{39}Ar loss by recoil.

Sample LM-DA-203 yielded a reliable minimum estimate for the intrusion age, derived from the analysis of magmatic amphibole-biotite aggregates. Encapsulated

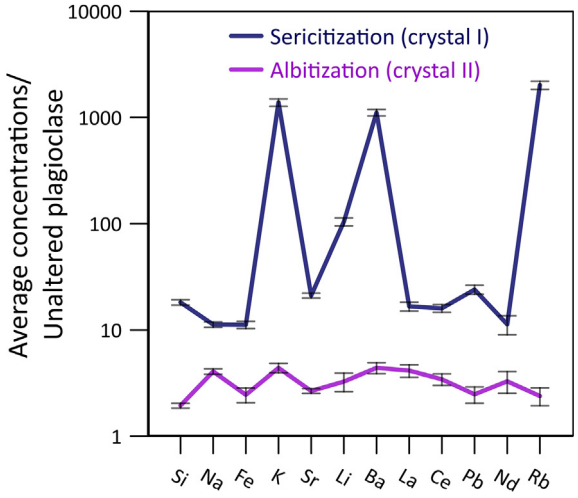

Fig. 5. Average element concentrations in alteration zones normalized by unaltered Ca-rich plagioclase average values. All data were extracted from selected regions in the LA-ICP-MS elemental maps through Monocle.

grain aliquots from sample LM-DA-203 (Fig. 7) failed to show significant ^{39}Ar contents in the first (piercing) step, indicating that the small grains did not release ^{39}Ar by recoil or heating during irradiation. The initial incremental-heating analysis of amphibole-biotite aggregates (Lab #9169, Fig. 7A) yielded a two-step flat segment comprising > 80% of the total ^{39}Ar released with the age of 132.33 ± 0.69 Ma. A second aliquot (#9170), analyzed with a more appropriate heating protocol, yielded a well-defined plateau containing 90% of the total ^{39}Ar released with the age of 132.20 ± 1.20 Ma (Fig. 7A). Both results are compatible with the combined isochron age of 132.83 ± 0.30 Ma (Fig. 7B; initial ^{40}Ar/^{36}Ar of 294.2 ± 1.2, within error of the present atmospheric value of 298.56 ± 0.31 of Lee et al., 2006).

Encapsulated grains of sericitized (cloudy) plagioclase from sample LM-DA-203 do not show evidence of ^{39}Ar release by recoil either. Incremental-heating analyses of two aliquots yielded reproducible spectra with old apparent ages in the initial steps that progressively descended towards well-defined plateaus containing more than 90% of the total ^{39}Ar released. The two encapsulated aliquots defined identical plateau ages of 107.28 ± 0.54 and 107.31 ± 0.52 Ma (Fig. 7C). An isochron for the entire data set yielded an age of 107.10 ± 0.23 Ma (Fig. 7D), within 2σ confidence level of the plateau ages, and showing an atmospheric initial ^{40}Ar/^{36}Ar value of 301.2 ± 1.1. These apparently coherent results are ~25 Ma younger than the plateau ages obtained for the magmatic amphibole-biotite clusters from the very same sample. Finally, sericite-free clear plagioclase crystals from sample LM-DA-203 yielded a spectrum with excess argon in low-temperature steps and a plateau at the high-temperature ones that comprised ~57% of the cumulative ^{39}Ar released and defined an age of 96.0 ± 1.20 Ma (Fig. 7E). The isochron fit by a positive elimination procedure to compensate for the excess Ar steps yielded a compatible age of 96.70 ± 1.60 Ma (Fig. 7F) and an initial ^{40}Ar/^{36}Ar value (296.5 ± 2.9) within 2σ from the present atmospheric value. The three apparently well-defined but totally distinct plateau ages obtained for the various minerals analyzed for mafic dyke LM-DA-203 clearly show the complexities associated with geochronology of partially altered mafic volcanic rocks, as discussed below.

Sample LM-DA-150 also shows complexity attributable to alteration. The sericitized plagioclase grains yielded a less pronounced saddle-shape spectrum with a well-defined plateau comprising more than 75% of total ^{39}Ar released and showing an age of 109.08 ± 0.45 Ma (Fig. 7G). The plateau age is compatible with the isochron age of 108.80 ± 0.26 Ma (Fig. 7H), showing that the plateau steps are not strongly affected by excess argon. In contrast, the sericite-free clear plagioclase grains from this sample display a pronounced saddle-shaped spectrum, showing significant excess argon (Fig. 7I) and minimum apparent ages at ~125 Ma.

All ^{40}Ar/^{39}Ar data are reported in supplementary material G. A combined probability density plot of the analyses exhibited in Fig. 7 is available in supplementary material L.

4.4. Bulk Rock Geochemistry and Sr-Nd isotope ratios

Bulk major and trace elements and Nd and Sr isotope results for each sample are reported in supplementary material H.

4.4.1. Major, minor and trace elements

All samples are basaltic and tholeiitic in composition (supplementary material I). The SiO_2 and MgO contents of the 11 dykes analyzed range between 48.0–48.9 and 8.4–7.0 wt%, respectively, and TiO_2 contents range from 1.0 to 1.9 wt% (Fig. 8). Loss on ignition varies from 0.3 to 1.4 wt%, showing that the whole-rock compositions are not strongly affected by weathering or post-magmatic hydration or carbonation. The alteration identified in the crystals is subtle, thus the difficulties in recognizing alteration and its effects on geochronology. All samples correspond to suite A (SiO_2 < 52 wt%, MgO > 5.5 wt%, most samples with Al_2O_3 < 14 wt%) of the tholeiitic dykes from CFTD as defined by Bennio et al. (2003). Major and minor element variation plots (Fig. 8) exhibit a typical tholeiitic crystallization sequence dominated by clinopyroxene and plagioclase and minor titanomagnetite fractionation: decrease in CaO and Al_2O_3 and increase in SiO_2, TiO_2, K_2O, Fe_2O_3t and P_2O_5 with decreasing MgO contents. Na_2O concentrations are notably scattered and do not exhibit any trends. Major and minor elements and do not exhibit any trend with LOI (Fig. 8).

Trace element plots versus MgO (Fig. 9) show progressive enrichment in La, Nd, Th and U as the magma evolves. Sr, Pb, and Ba concentrations also increase, despite some scatter, while Rb does not exhibit any particular trend.

To further characterize anomalies in whole-rock data, we plotted minor and trace elements against three different proxies: La (which, in Fig. 9, follows a normal magmatic evolution pattern and does not seem to have been considerably disturbed by post-magmatic events); K (which is

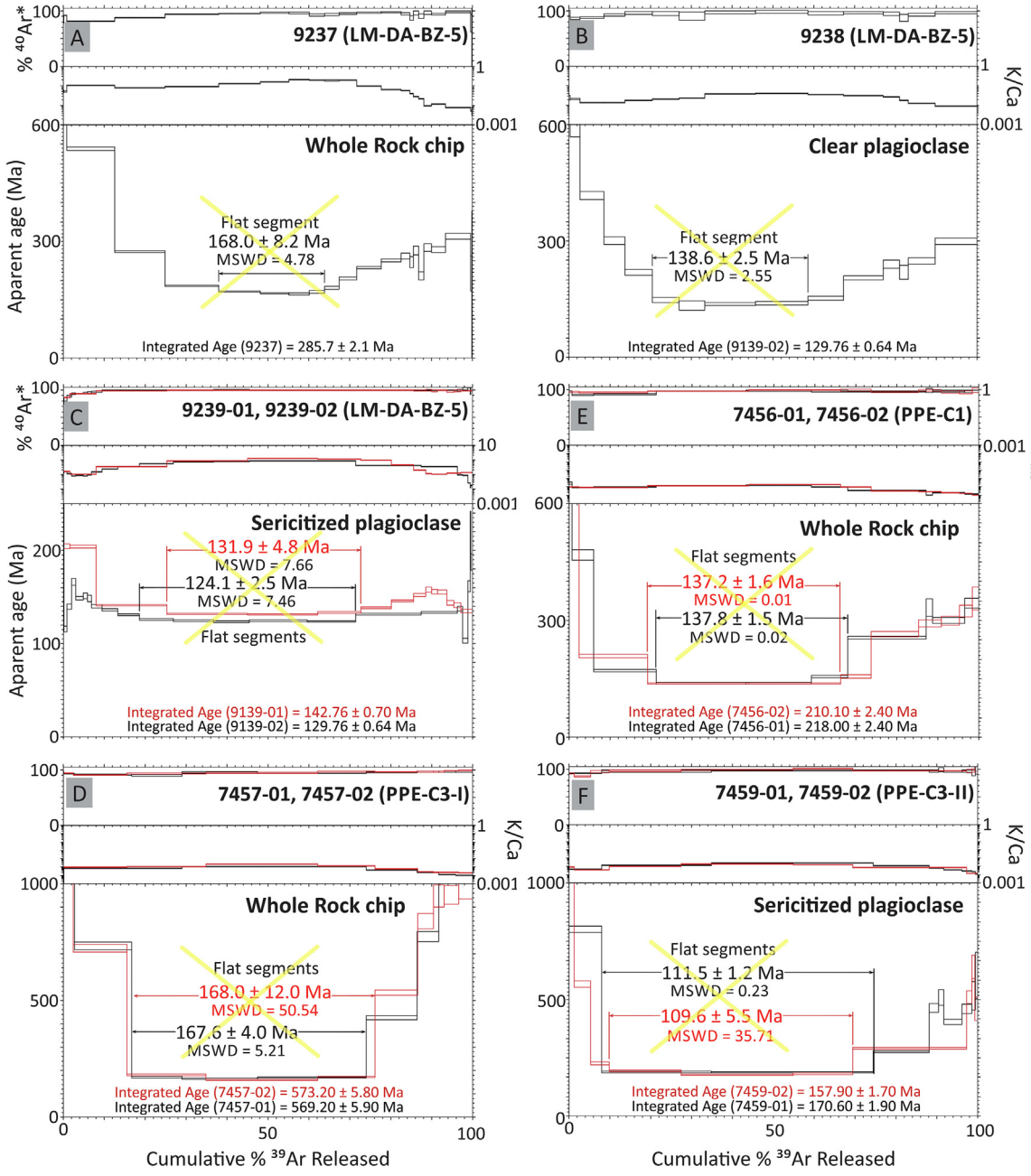

Fig. 6. $^{40}Ar/^{39}Ar$ geochronology results (age spectra) of whole-rock (A), clear (B) and cloudy (sericitized) (C) plagioclase crystals from dyke LM-DA-BZ-5 (#9237, #9238, #9239–01 and −02), and of whole-rock (D and E) and cloudy (sericitized) (F) plagioclase crystal from dyke PPE-C (#7456–01 and −02, #7457–01 and −02 and 7459–01 and −02). None of the results above is a proper age, and they should not be interpreted as such (thus, the crosses over the diagrams).

present in sericitized and albitized zones of plagioclase crystals); and LOI (a proxy for volatile input during hydrothermal alteration or weathering). All plots are shown in Fig. 10. Th, U and Na increase with La increase, whereas Sr does not follow any trend. Rb, also enriched in altered zones of the plagioclase crystals, increases as K increases. Sr and Pb do not show defined trends when plotted against LOI.

Rare earth element (REE) patterns normalized to CI chondrite (McDonough and Sun, 1995) and multi-element patterns normalized to primitive mantle (McDonough and Sun, 1995) are shown in Fig. 11. The diagrams include CFTD data from Bennio et al. (2003) and Almeida et al. (2021), and Esmeralda and Ribeira basalts (Peate, 1997; Marques et al., 1999, and references therein), two subgroups of the Paraná-Etendeka Magmatic Province that display low TiO_2 contents, similarly to the CFTD dykes.

Enrichment in light REE is observed for all samples ($2.1 \leq (La/Lu)_{CN} \leq 4.0$, mean $= 2.7 \pm 0.3$; $1.4 \leq (La/Sm)_{CN} \leq 2.7$, mean $= 1.8 \pm 0.2$). Additionally, most of the samples

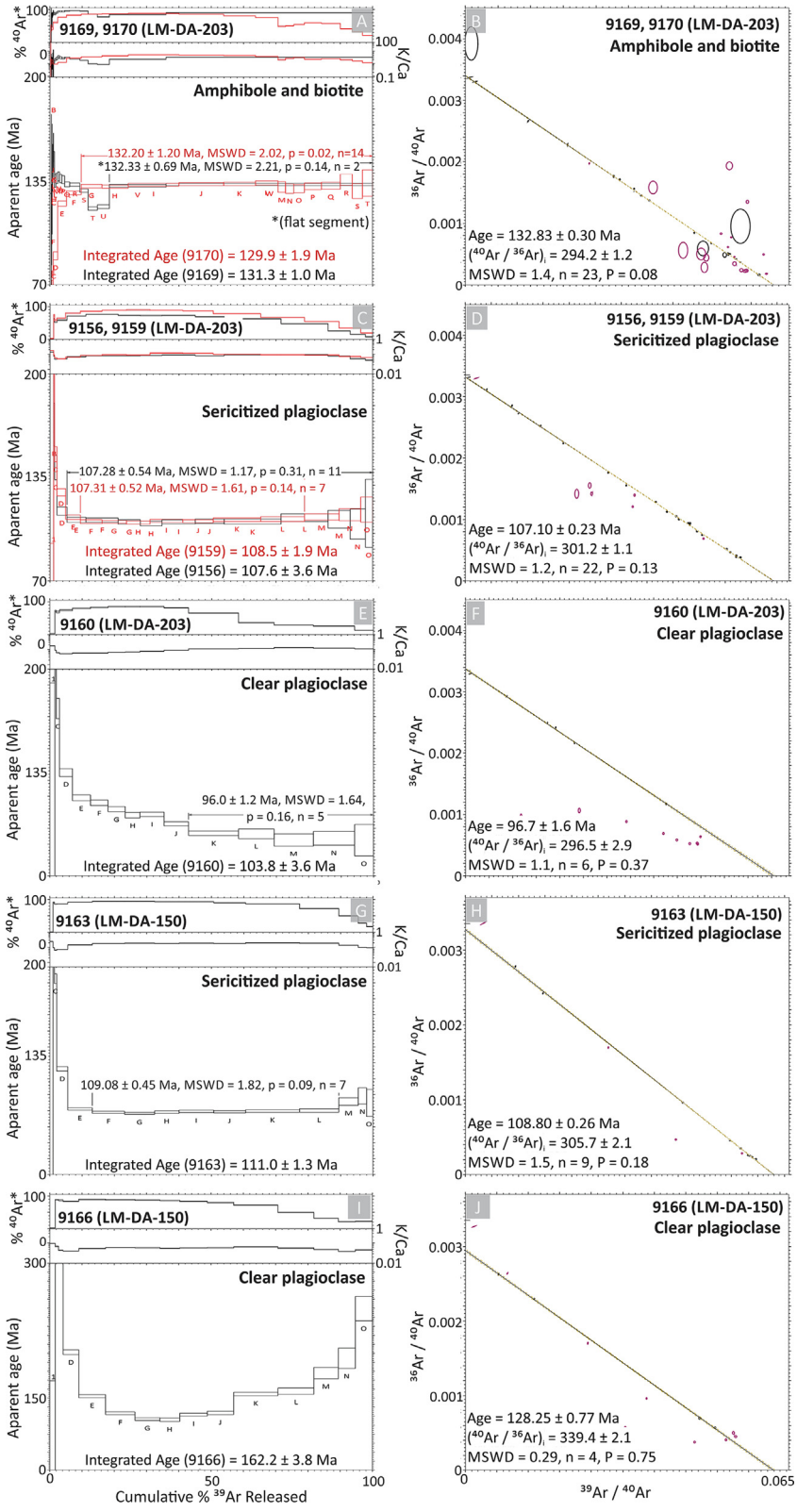

Fig. 7. $^{40}Ar/^{39}Ar$ geochronology results (age spectra, isochrons and probability density plots) of samples LM-DA-203 (A-I; #9169, #9170, #9156, #9159 and #9160) and LM-DA-150 (J-O; #9163 and #9166).

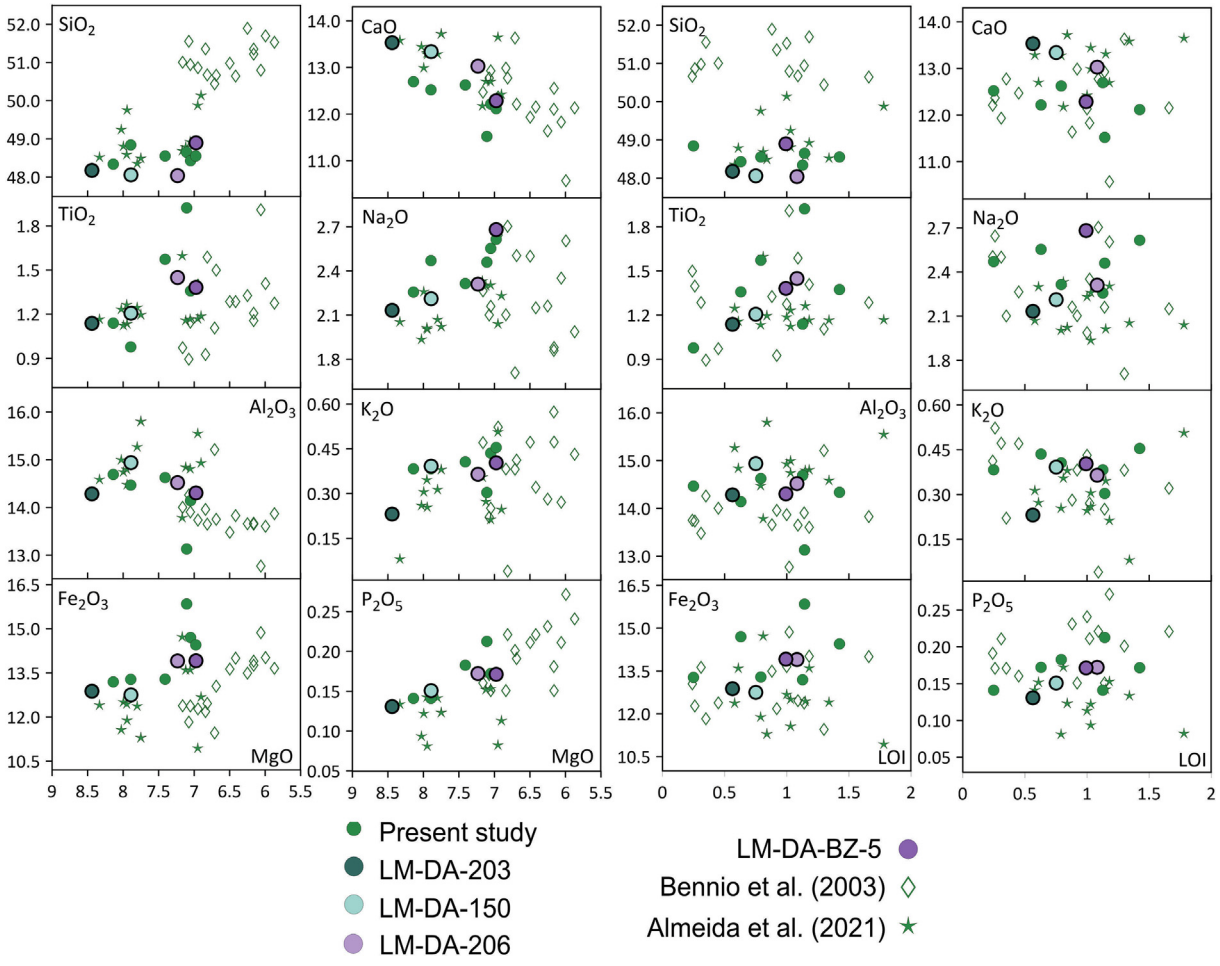

Fig. 8. Major and minor elements (wt%, on dry basis) vs. MgO (wt%) and vs. LOI (wt%). Circles represent samples from this study. Samples LM-DA-203, LM-DA-150, LM-DA-BZ-5 and LM-DA-206 are highlighted (the first three were dated, and all of them have Sr and Nd isotope data). Empty diamonds consist of samples from Bennio et al. (2003), and stars are from Almeida et al. (2021), whenever available.

show slightly positive Eu anomalies ($0.92 \leq Eu/Eu^* \leq 1.11$, mean = 1.03 ± 0.04; Eu/Eu* is defined by $Eu_{CN}/\sqrt{Sm_{CN}.Gd_{CN}}$). In the primitive mantle normalized multi-element diagram the dykes show erratic anomaly patterns (especially for Rb, Ba, K and Pb), similarly to those observed in Figs. 9 and 10, and consistent with mobility of these elements during alteration. In contrast, normalized Nb/Ta and Th/Nb values do not exhibit large variation ($0.84 \leq (Nb/Ta)_{PM} \leq 1.08$, mean 0.95 ± 0.04; $0.83 \leq (Th/Nb)_{PM} \leq 1.45$, mean 0.99 ± 0.06). All dykes have slightly negative Ti values.

4.4.2. Sr and Nd isotope compositions

Initial Sr and Nd isotope ratios were calculated (supplementary material H) using the 132.32 ± 0.48 Ma $^{40}Ar/^{39}Ar$ age obtained for the amphibole-biotite aliquots, our best estimate for the age of dyke emplacement (Fig. 7C). The dykes have initial $^{87}Sr/^{86}Sr$ ratios varying from 0.70377 to 0.70429, and initial $^{143}Nd/^{144}Nd$ ranging between 0.51256 and 0.51264. Initial Sr and Nd isotope ratios are plotted along with previous results by Bennio et al. (2003) and LTi Esmeralda and Northern Paraná-Etendeka Magmatic Province basalts from South America (subgroup Ribeira is included; Fig. 12A and 13; Peate, 1997; Marques et al., 1999; Rocha-Júnior et al., 2013, 2020; and references therein). Initial $^{87}Sr/^{86}Sr$ vs MgO (Fig. 12B) is also shown.

In $^{87}Sr/^{86}Sr$ and $^{143}Nd/^{144}Nd$ diagrams (Fig. 12A), the dykes plot in the same field of primitive group A defined by Bennio et al. (2003) and display lower $^{87}Sr/^{86}Sr$ and higher $^{143}Nd/^{144}Nd$ than Esmeralda and Northern Paraná-Etendeka Magmatic Province basalts. $^{87}Sr/^{86}Sr$ values do not correlate with MgO contents (Fig. 12B).

5. DISCUSSION

5.1. Interpreting complex $^{40}Ar/^{39}Ar$ geochronological results

The wide range and complexity of geochronological results obtained for both whole rock fragments and plagioclase crystals (between apparent ages of ~168 Ma for saddle-shaped spectra and true plateau age of 96.0 ± 1.20 Ma for an albitized plagioclase crystal) illustrate the challenges associated with dating mafic dyke swarms from southeastern Brazil. Rigorous interpretation is essential

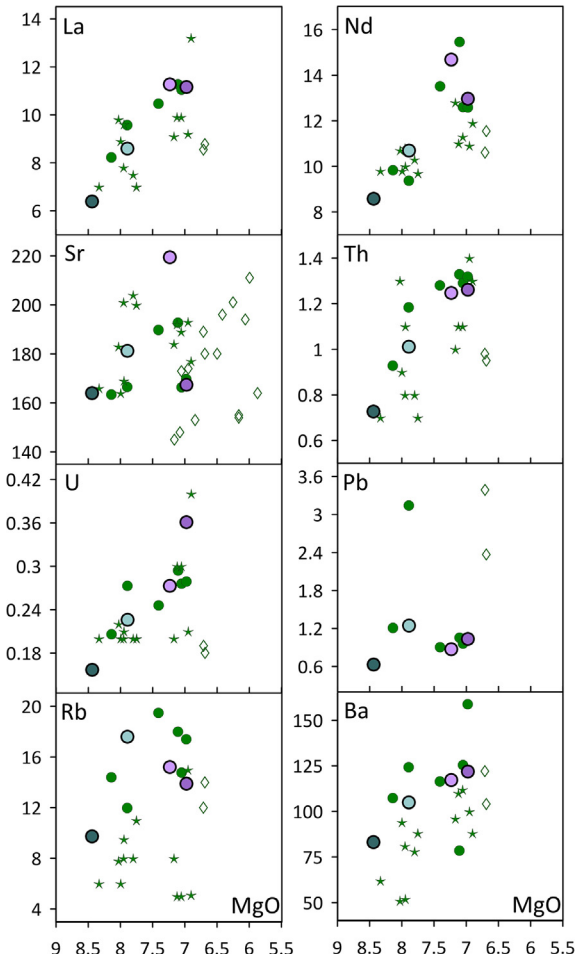

Fig. 9. Trace element (ppm) vs. MgO (wt%, on dry basis). Symbols as in Fig. 8.

for differentiating intrusion ages from geochronological artefacts (e.g., excess argon) or post-intrusion alteration.

5.1.1. Saddle-shaped incremental-heating spectra

Every whole-rock fragment analyzed in this study (samples LM-DA-BZ-5, PPE-C1, PPE-C3-I) yielded saddle-shaped spectra that reveal the presence of significant excess argon components (Fig. 6). Even though the saddle-shaped spectra reach flat segments at the middle temperature steps, none of these segments provides reliable geochronological information because of the large amounts of excess argon.

Saddle-shaped spectra are not confined to whole-rock fragments. Pristine (sample LM-DA-BZ-5, Fig. 6B; sample LM-DA-150, Fig. 7I) and sericitized plagioclase crystals (sample LM-DA-150, Fig. 7G; sample LM-DA-BZ-5, Fig. 6C; and sample PPE-C3-II, Fig. 6F) also yielded saddle-shaped spectra, showing that excess argon is pervasive throughout the dykes and cannot be necessarily obviated by dating plagioclase phenocrysts. The excess argon component is more pronounced in the center than the margins of the dykes.

The large amounts of excess argon (high apparent ages in low and high temperature steps) in whole-rock fragments and plagioclase crystals suggest that dyke emplacement occurred at depth, without major exchanges with crustal fluids or the atmosphere (McDougall and Harrison, 1999). The abundance of excess argon in the dykes makes it difficult to use the $^{40}Ar/^{39}Ar$ incremental-heating results at face-value. Importantly, the fact that many of the published $^{40}Ar/^{39}Ar$ results for southeastern Brazil mafic dykes reveal similar saddle-shaped spectra (e.g., Bennio et al. 2003; Guedes et al., 2005, 2016; Almeida et al., 2021) suggests that the true age of magma emplacement in these systems may yet to be determined.

5.1.2. Age of magmatism

Among the four mafic dykes investigated in this study (samples LM-DA-BZ-5, LM-DA-150, LM-DA-203, PPE-C), only magmatic amphibole-biotite grains from sample LM-DA-203 (Fig. 7A, B) provide reliable information about the age of magmatism. The well-defined plateau of aliquot #9170, compatible with the large flat segment of aliquot #9169, the absence of ^{39}Ar recoil losses from the small crystals, the reproducibility of results for the two aliquots, the absence of excess argon (Fig. 7B), combined with the high closure temperatures for amphibole suggest that 132.83 ± 0.30 Ma (isochron age) is a reliable age of crystallization of the amphibole-biotite clusters. The minerals result from late-stage magmatic alteration of pyroxene, implying that 132.83 ± 0.30 Ma is the minimum age of magmatic intrusion. All other attempts at geochronology yielded results affected by excess argon or alteration.

5.1.3. $^{40}Ar/^{39}Ar$ results for sericitized plagioclase crystals

Cloudy plagioclase crystals from the CFTD mafic dykes invariably reveal young ages, but most of these cloudy plagioclase crystals also show some excess argon. Fortunately, some samples (e.g., sample LM-DA-203, Fig. 7C; sample LM-DA-150, Fig. 7G) show that sericitization may be so pervasive that it overwhelms the excess argon component in the sericitized plagioclase crystals, suggesting that incremental-heating ages may indeed record the timing of pervasive K-alteration of the mafic dykes.

Cloudy plagioclase crystals from dyke LM-DA-203 yield reproducible plateau ages of 107.28 ± 0.54 and 107.31 ± 0.52 Ma (Fig. 7C), which most likely record the maximum age of sericitization. Cloudy plagioclase crystals from dyke LM-DA-150, located ~20 km away from LM-DA-203, record a maximum age of sericitization of 109.08 ± 0.45 Ma (Fig. 7G). Finally, two sericitized plagioclase crystals from dyke PPE-C3-II, located ~5 km away from LM-DA-203 (Fig. 1), failed to produce age plateaus but yielded two flat segments, containing more than 50% of the total ^{39}Ar released, that suggest apparent age estimates of 111.5 ± 1.2 and 109.6 ± 5.5 Ma. Ages obtained from sericitized plagioclase crystals record noble gas contributions from two distinct reservoirs: sericite crystals and unaltered plagioclase remnants. Therefore, apparent differences in sericitization ages among dykes LM-DA-203, LM-DA-150, and PPE-C3-II may simply reflect differences in the percentages of the original plagioclase crystals that survived alteration. The similar ages for sericitized plagioclases from

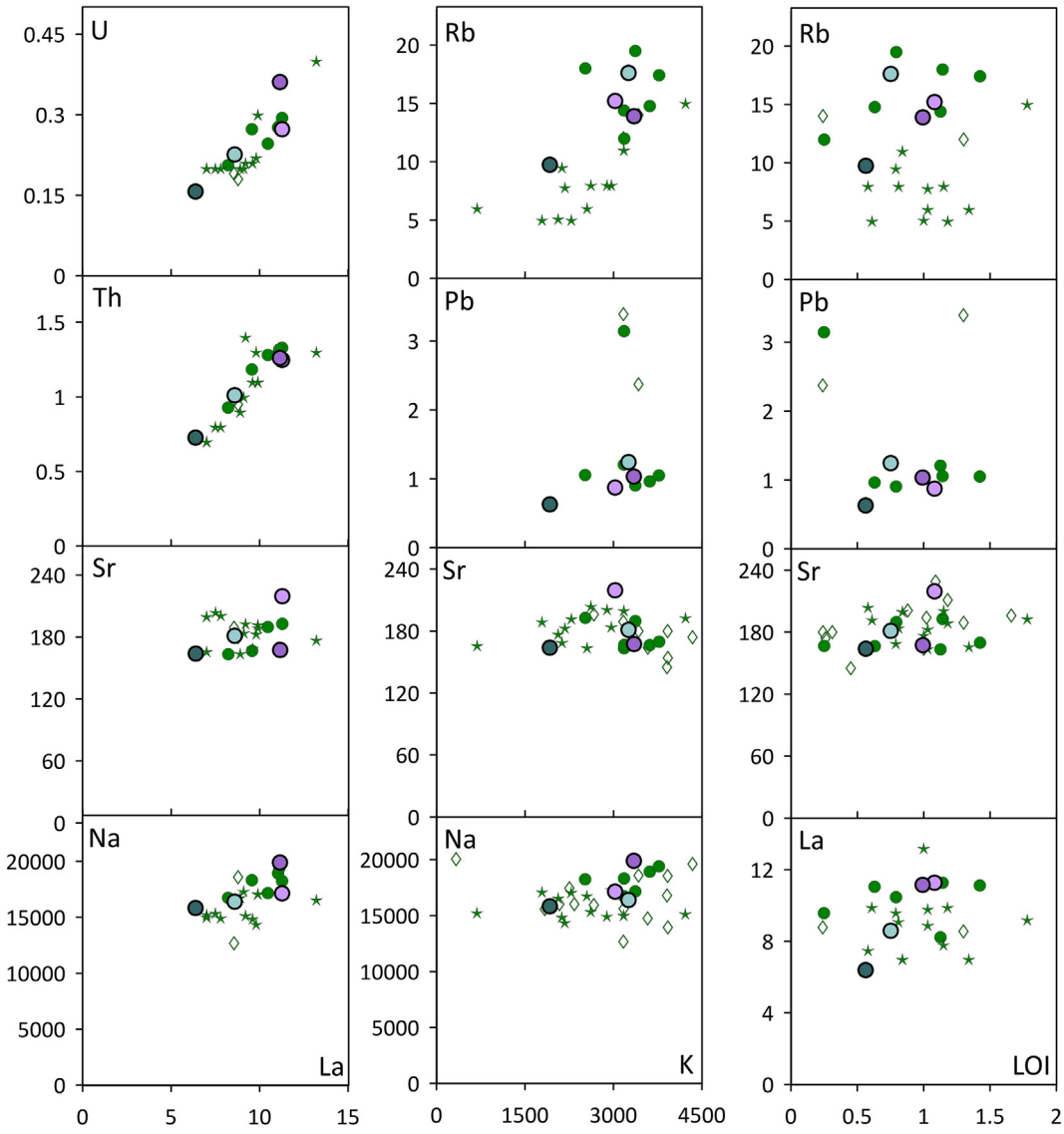

Fig. 10. Minor and trace element plots vs. La and K concentrations (ppm) and LOI (wt%). Symbols as in Fig. 8.

three dykes up to 25 km apart suggest that the K-rich fluid that altered Ca-rich plagioclase phenocrysts to sericite travelled through extensive parts of the crust.

The reproducible and flat spectra for the two sericitized plagioclase aliquots from dyke LM-DA-203, and the apparent absence of an excess argon component, suggest that the isochron age of 107.10 ± 0.23 (Fig. 7D) Ma is a reliable age for the K-alteration event that affected the mafic dykes in the CFTD. However, a more robust estimate of the sericitization age was obtained by a mixture model (Fig. 13A, outlined in supplementary material J), analogous to the one proposed by Verati and Jourdan (2014). The model estimates the amount of radiogenic ^{40}Ar generated from a pure igneous ~132 Ma plagioclase (K by EPMA = 0.008 mol) mixed with sericite (K by EPMA = 0.602 mol) of several possible ages. Given that petrographic observations and LA-ICP-MS elemental analyses reveal ~15–25% sericitization, the age of 107.10 ± 0.23 Ma is a maximum age for the alteration and probably reflects a mixture of ~80% 132 Ma plagioclase with ~20% of a sericite generation ~106–105 Ma (Fig. 13A). The mixture model can also predict the K/Ca ratios obtained for the sericitized plagioclase during step-heating analysis, which range between 0.1 and 1 (Fig. 14).

5.1.4. $^{40}Ar/^{39}Ar$ results for albitized plagioclase crystals

The low K-contents of magmatic plagioclase measured for the Cabo Frio dykes also make them very susceptible to age resetting by the introduction of Na and minor K during albitization. A visually "fresh" plagioclase crystal from the same LM-DA-203 sample yielded a plateau age of 96.0 ± 1.20 Ma (Fig. 7E). The age spectrum has a prominent slope, suggesting that the results may be affected by excess Ar. However, the plateau steps have no resolvable slope (Sharp and Renne, 2005; Schaen et al., 2020), and the excess Ar and plateau trends are distinguishable in the isochron (Fig. 7F), which allows us to estimate a maximum age of alteration.

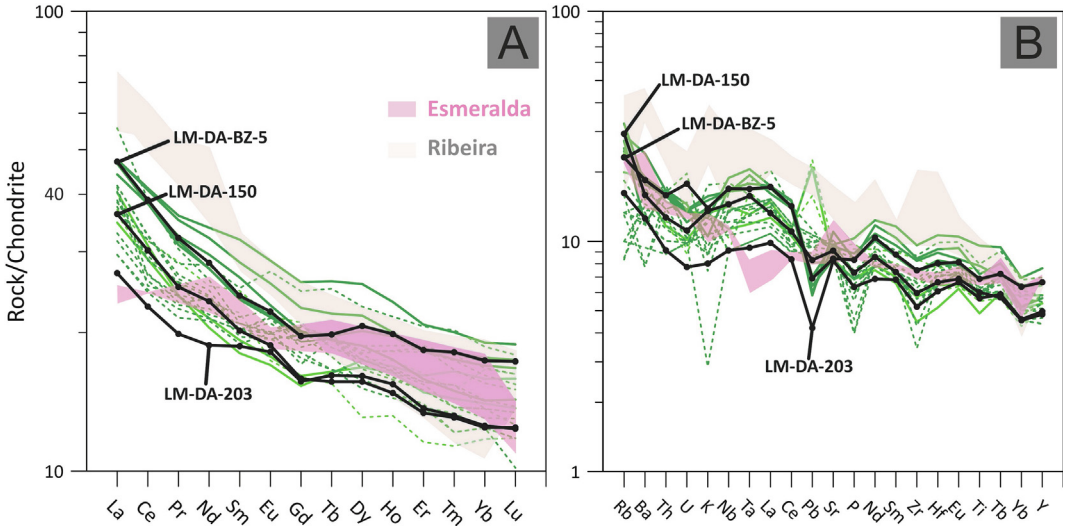

Fig. 11. A- CI-normalized (McDonough and Sun, 1995) REE patterns of group A (defined by Bennio et al., 2003). Samples LM-DA-203, LM-DA-150 and LM-DA-BZ-5 are highlighted. The results reported by Bennio et al. (2003) and by Almeida et al. (2021) are shown as dashed lines. LTi Esmeralda and Ribeira basalt samples from Paraná-Etendeka Magmatic Province are also illustrated (Peate, 1997; Marques et al., 1999; references therein). B - Primitive mantle normalized (McDonough and Sun, 1995) multi-element patterns of group A.

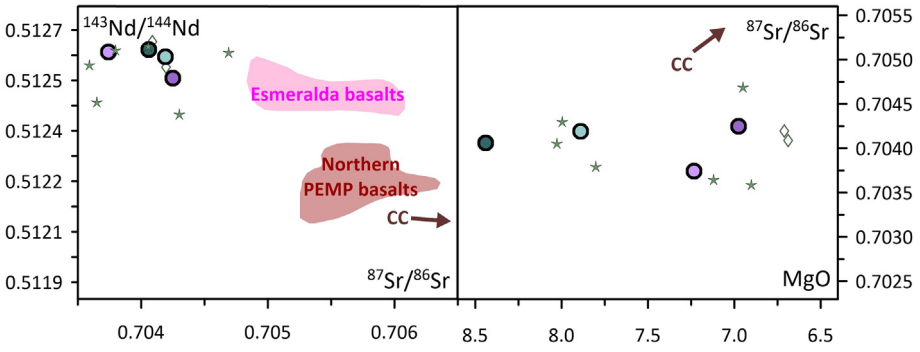

Fig. 12. A - Initial $^{87}Sr/^{86}Sr$ and $^{143}Nd/^{144}Nd$ compositions of mafic CFTD dykes, along with LTi and Northern basalt flows from the South American Paraná-Etendeka Magmatic Province (Peate, 1997; Marques et al., 1999; Rocha-Júnior et al., 2013, 2020; Machado et al., 2015; and references therein). CC – Regional continental crust (average $(^{87}Sr/^{86}Sr)_{133Ma} = 0.7125$; $(^{143}Nd/^{144}Nd)_{133Ma} = 0.5121$; MgO = 1.95 wt%; Peixoto et al., 2017). B – Initial $^{87}Sr/^{86}Sr$ vs. MgO (wt%) distribution shows little variation with MgO decrease.

LA-ICP-MS elemental maps show that the sample was albitized. Electron microprobe analyses show that hydrothermal albite contains ~0.025 mol K, as compared to 0.007 mol K in the original plagioclase phenocrysts, revealing that K was introduced together with Na during albitization. Fig. 13B illustrates the effect of various proportions of albitization, at different times (90, 80, 70, 60, 50, 40 and 30 Ma), on the apparent age measured for the plagioclase phenocryst. Based on SEM observations, LA-ICP-MS elemental maps, and electron microprobe analysis, visual estimation of the plagioclase phenocrysts albitization varies between ~10–30 wt%. Therefore, albitization must have occurred sometime between 60 and 30 Ma. Once again, the mixing model is coherent with the K/Ca ratios measured during step-heating analysis, which range between 0.01 and 0.1 (Fig. 14).

The 60–30 Ma period corresponds to the emplacement of late-stage alkaline magmatism along the Cabo Frio Lineament, which connects Poços de Caldas and Cabo Frio by a series of intrusions (Fig. 1; Ferroni et al., 2017, and references therein). The age similarity suggests possible links between thermal anomalies induced by the alkaline magmatism and circulation of hydrothermal solutions along coastal dykes and fracture zones.

Albitization of plagioclase crystals can also explain the difficulties in obtaining reproducible $^{40}Ar/^{39}Ar$ ages from various aliquots from a same sample from the Cabo Frio Tectonic Domain dykes, as illustrated in Almeida et al. (2021). Age differences among visually pristine crystals from a same intrusion probably result from variable proportions of hydrothermal albite, which is not readily identifiable by optical microscopy.

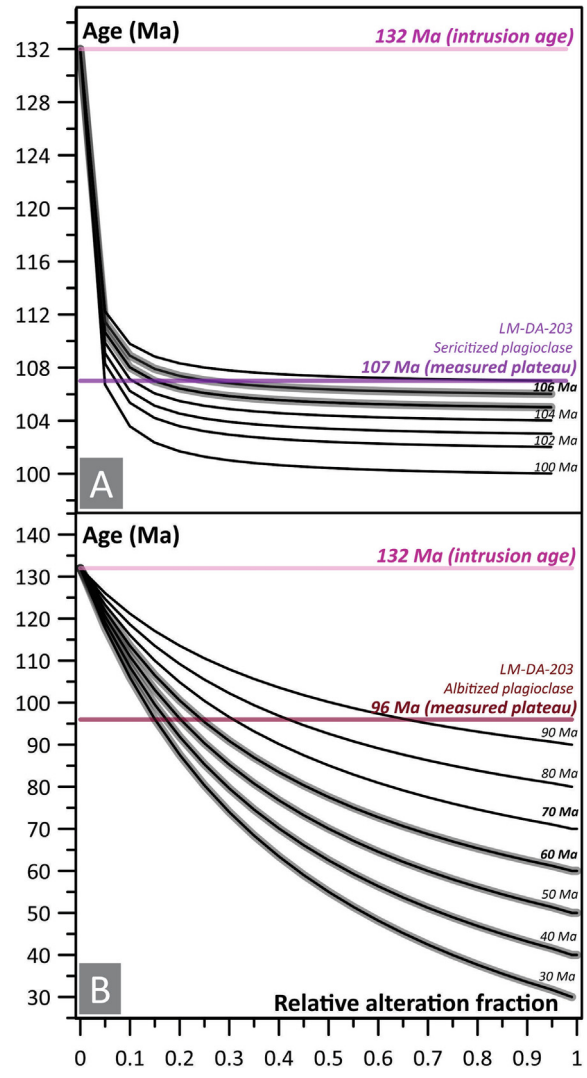

Fig. 13. Modeled ages (black lines) for sample LM-DA-203 of mixtures between pristine bytownitic plagioclase and an alteration phase, either sericite (A) and albite (B), of various ages. The intercepts between modeled ages and measured plateau ages indicate the needed proportion of an alteration phase of a given composition and age. Approximately 10–20 wt% of 106–105 Ma sericite mixed with bytownitic plagioclase would produce the observed plateau age. Similarly, approximately 10–20 wt% of 40 to 70 Ma albite would suffice to produce the measured ~96 Ma plateau age.

5.2. Effects of hydrothermal activity on geochemical and isotopic compositions: implications to fluid sources and tectonic evolution

$^{40}Ar/^{39}Ar$ geochronology shows that both sericitization (~106–105 Ma; Fig. 13A) and albitization (60–30 Ma; Fig. 13B) disturbed the K-Ar system in some of the plagioclase crystals from the CFTD dykes. The LA-ICP-MS and whole-rock geochemistry results provide further evidence for alteration: many of the elements (e.g., K, Na, Pb, Sr, Rb, Ba) present in sericitized and albitized areas of plagioclase crystals are scattered when plotted against MgO contents for whole-rock data. These elements increase with

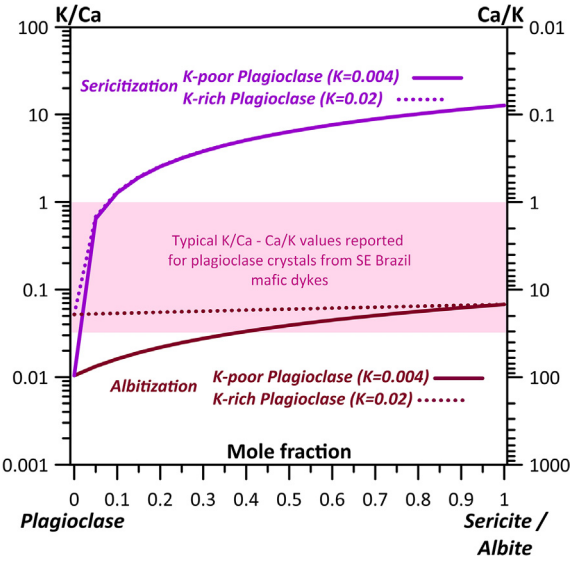

Fig. 14. K/Ca and Ca/K ratios for different mole fractions of K-poor and K-rich plagioclase and sericitization/albitization (all calculations are available in supplementary material J).

increasing K contents (Fig. 10). Combining all geochemical proxies permits evaluating possible sources of alteration fluids.

Firstly, the elements enriched in the altered samples (e.g., K, Na, Rb, Sr, Li, Ba) are readily soluble in and removed by weathering solutions, confirming that weathering is not the process responsible for affecting the K-Ar system. The absence of major and trace element correlations with LOI values (Figs. 8, 10) is further evidence that weathering processes, which typically result in high LOI values, have not significantly affected the dyke samples.

Similarly, seawater input was not significant because the LREE enrichment and HREE depletion in the sericitized and albitized zones of plagioclase crystals is the opposite of what would be expected if seawater was involved (e.g., Elderfield, 1988; Zheng et al., 2016; Deng et al., 2017). In addition, $^{87}Sr/^{86}Sr$ values for the least radiogenic sample of the set vs 1/Sr concentrations do not follow a mixing trend with Albian seawater (Veizer, 1989; Fig. 15).

The absence of Sr and Nd trends towards local crustal compositions (Fig. 12; data from Peixoto et al., 2017) suggests that crustal fluids were not significant in the alteration of the dykes.

Late-stage magmatic liquids, which affected some of the primary clinopyroxene and olivine crystals and generated amphibole, biotite and chlorite, could have supplied the incompatible elements to the altering feldspars. However, the sericitization and albitization ages suggest that fluid percolation took place long after the deuteric processes which resulted in the 132.83 ± 0.30 Ma magmatic amphiboles-biotites clusters (Fig. 7B), also precluding the involvement of magmatic fluids in the alteration processes.

Furthermore, the $^{40}Ar/^{39}Ar$ results suggest that sericitization and albitization occurred at different times and involved distinct solution compositions. Sericitization solutions (Fig. 3,5) were enriched in K, Na, Si, Rb, Ba, Pb, Sr, Li and some LREE (La, Ce, minor Nd). In contrast, albiti-

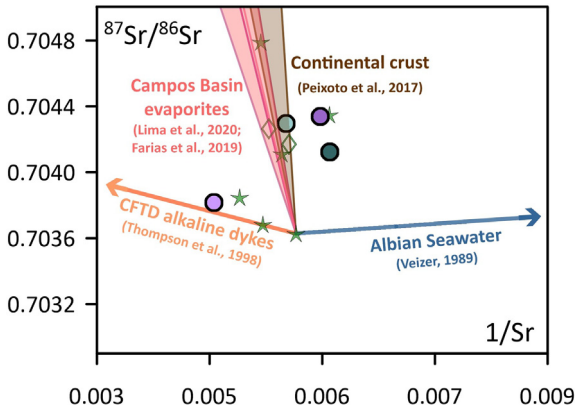

Fig. 15. Initial $^{87}Sr/^{86}Sr$ versus 1/Sr concentrations for the Cabo Frio Tectonic Domain (CFDT) dykes. Mixing curves between the least radiogenic sample of the set and Albian seawater (Veizer, 1989), CFTD alkaline dykes (Thompson et al., 1998), Campos Basin evaporites (Farias et al., 2019; Lima et al., 2020) and regional continental crust (Peixoto et al., 2017) are indicated. All isotopic data was corrected to 100 Ma. Symbols as in Fig. 12.

zation solutions (Figs. 4, 5) were not rich in Si, Pb and REE and were less enriched in K, Fe, Sr, Li, Ba and Rb than sericitization solutions. This change in composition of the percolating fluids may reflect distinct source compositions or PT conditions (Warren, 2016).

Alteration ages indicate that fluid percolation was coeval with alkaline magmatism along the southeastern margin of Brazil, which started at 134 Ma and occurred, episodically, until about 60–50 Ma (Montes-Lauar et al., 1995; Gomes et al., 2018; Ferroni et al., 2017; and references therein; Gomes and Vasconcelos, 2021). These magmas intruded both continental onshore basement and adjacent offshore sedimentary basins, suggesting that some of the geochemical characteristics of the alteration fluids may have been derived from water-rock interactions in these offshore basins.

The South Atlantic marginal basins are notorious for extensive and thick evaporite layers formed during the late Aptian (Milani and Filho, 2000). Seismic reflection (Magee et al., 2021) show that Late Cretaceous and Paleogene magmatism intruded and interacted with the Aptian salt layers, causing hydrothermal circulation and Albian-Santonian salt movement. If these layers were to be partially dissolved during alkaline magmatism, hot solutions rich in K and Na would be produced and could have migrated into the extending tectonic margin, interacting with alkaline pulses, basement rocks and seawater, particularly when lithospheric uplift and extension were enhanced after the Aptian-Albian transition (Cogné et al., 2012; Granot and Dyment, 2015). The increase and scatter of $^{87}Sr/^{86}Sr$ data of the tholeiitic dykes can be explained by mixing curves involving evaporitic compositions of the Campos Basin (in the immediate offshore of Cabo Frio Tectonic Domain; Farias et al., 2019; Lima et al., 2020) and variable smaller contributions of regional continental crust (Peixoto et al., 2017), regional alkaline dykes (Thompson et al., 1998) and perhaps a minor Albian seawater component (Fig. 15).

A schematic illustration of how hydrothermal cells may have driven sericitization and albitization along the margin is depicted in Fig. 16. If proven correct, these hydrothermal cells may have affected the rheological properties and geochemical characteristics of the rifting margin. Furthermore, if the hydrothermal alteration processes identified in the Cabo Frio Tectonic Domain occurred along the entire South Atlantic coast, young mafic dykes elsewhere in southeastern Brazil (e.g., Renne et al., 1996; Deckart et al., 1998; Raposo et al., 1998; Guedes et al., 2016; Almeida et al., 2021) may also have partial resetting of the K-Ar system. Systematic elemental mapping of plagioclase crystals used in geochronology would permit testing this hypothesis.

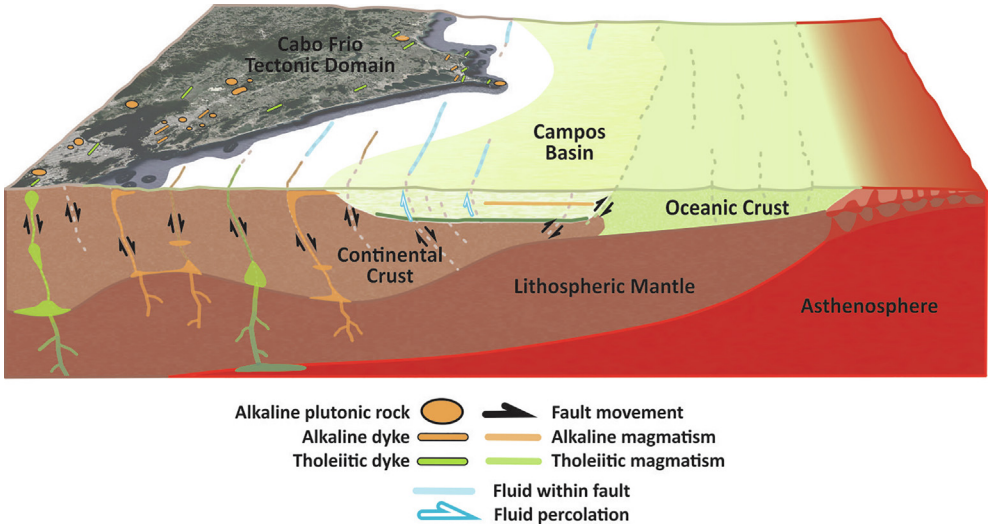

Fig. 16. Hydrothermal fluid percolation affecting the Cabo Frio Tectonic Domain at ~106–105 Ma. Similar processes occurred again between 60–30 Ma. Fluids generated in evaporite-rich marginal basin (Campos Basin) percolated the crust through extensional faults, partially altering the intrusive rocks emplaced along the same faults during Gondwana breakup and South Atlantic opening.

6. CONCLUSIONS

$^{40}Ar/^{39}Ar$ analyses of encapsulated amphibole and biotite crystals from primitive mafic dykes from the Região dos Lagos, Cabo Frio Tectonic Domain, southeastern Brazil, yielded a minimum intrusion age of 132.83 ± 0.30 Ma (1σ), which corresponds to early stages of Gondwana breakup and South Atlantic expansion. LA-ICP-MS elemental maps of altered plagioclase crystals from the same samples unveil the passage of fluids enriched in K, Na, Rb, Ba, Sr, Si, Li, Fe, Pb and light REE that affected the K-Ar system. Analyses of encapsulated sericitized plagioclase crystals suggest alteration by K-rich fluids at ~106–105 Ma; albitized plagioclase crystals suggest migration of Na-rich fluids in the 60–30 Ma interval.

Trace element and isotopic data suggest that the tholeiitic mafic magmas were not significantly contaminated by the continental crust or seawater. Instead, alkaline magmatic intrusions into evaporite layers in the marginal basins likely mobilized Na- and K- rich fluids and introduced them into the expanding crust. These hydrothermal processes led to albitization and sericitization that affected the K-Ar system in the Cabo Frio Tectonic Domain mafic dykes. Similar processes may have also partially reset the K-Ar system in a number of other dyke swarms in southeastern Brazil and Africa.

Declaration of Competing Interest

The authors declare that they have no known competing financial interests or personal relationships that could have appeared to influence the work reported in this paper.

ACKNOWLEDGEMENT

This research was supported by Fundação de Amparo à Pesquisa do Estado de São Paulo (FAPESP; Procs. 2012/06082-6, 2014/22948-9, 2017/18232-6, 2018/23650-4), Petrobras, Coordenação de Aperfeiçoamento de Pessoal de Nível Superior (CAPES; Proc. 1425945), and Conselho Nacional de Desenvolvimento Científico e Tecnológico (CNPq; Proc. 141058/2018-8). The Argon Laboratory at UQ-AGES was partially funded byARC Large grant A39531815 to PV, and the 40Ar/39Ar, microscopy and EPMA, and LA-ICP-MS analysis were funded by UQ-AGES. We thank Marcia Ernesto, Fábio Braz Machado and Caio Morelli Vicentini for all the assistance and orientation during sampling. We are also very thankful to Liliane Aparecida Petronilho, David Thiede, Allan Gomes, Alice Mcdonald and Al-Tamini Tapu for suggestions and support during analyses. The authors acknowledge the facilities and the scientific and technical assistance of the Microscopy Australia Facility at the Centre for Microscopy and Microanalysis (CMM), The University of Queensland. LS Marques and M Babinski are CNPq Fellow Researchers. Fred Jourdan, Renaud Merle, Arto Luttinen, Courtney Sprain and Brian Jicha are acknowledged for insightful suggestions on the manuscript.

REFERENCES

Almeida J., Dios F., Mohriak W. U., Valeriano C. D. M., Heilbron M., Eirado L. G. and Tomazzoli E. (2013) Pre-rift tectonic scenario of the Eo-Cretaceous Gondwana break-up along SE Brazil–SW Africa: insights from tholeiitic mafic dyke swarms. *Geol. Soc. London Spec. Publ.* **369**, 11–40.

Almeida J., Heilbron M., Guedes E., Neubauer F., Manfred B., Klausen M. B., Valeriano C. M., Bruno H., Giro J. P., McMaster M. and Tetzner W. (2021) Pre-to-syn tholeiitic magmatism in a transtensive hyperextended continental margin: Onshore and offshore magmatism of the Campos Basin, SE Brazil. *J. South Am. Earth Sci.* **108** 103218.

Assumpção M., Marza V., Barros L., Chimpliganond C., Soares J. E., Carvalho J., Caixeta D., Amorin A. and Cabral E. (2002) Reservoir induced seismicity in Brazil. *Pure Appl. Geophys.* **159**, 597–617.

Baksi A. K. and Archibald D. A. (1997) Mesozoic igneous activity in the Maranhão province, northern Brazil: 40Ar/ 39Ar evidence for separate episodes of basaltic magmatism. *Earth Planet. Sci. Lett.* **151**(3/4), 139–153.

Bellieni G., Montes-Lauar C. R., De Min A., Piccirillo E. M., Cavazini G., Melfi A. J. and Pacca I. G. (1990) Early and Late Cretaceous magmatism from São Sebastião island (SE-Brazil): geochemistry and petrology. *Geochim. Bras.* **4**(1), 59–83.

Bennio L., Brotzu P., D'Antonio M., Feraud G., Gomes C. B., Marzoli A., Melluso L., Morbidelli L., Morra V., Rapaille C. and Ruberti E. (2003) The tholeiitic dyke swarm of the Arraial do Cabo peninsula (SE Brazil): $^{39}Ar/^{40}Ar$ ages, petrogenesis, and regional significance. *J. South Am. Earth Sci.* **16**, 163–176.

Cogné N., Gallagher K., Cobbold P. R., Riccomini C. and Gautheron C. (2012) Post break-up tectonics in Southeast Brazil from thermochronological data and combined inverse-forward thermal history modeling. *J. Geophys. Res.* **117**, B11413.

Corval A., Valente S. C., Duarte B. P., Famelli N. and Zanon M. (2008) Dados petrológicos dos diabásios dos setores centro-norte e nordeste do Enxame de Diques da Serra do Mar. *Geochim. Bras.* **22**(3), 159–177.

Cotta A. and Enzweiler J. (2008) Certificate of Analysis of the Reference Material BRP-1 (Basalt Ribeirão Preto). *Geostand. Geoanal. Res.* **32**, 231–235.

Deckart K., Féraud G., Marques L. S. and Bertrand H. (1998) New time constraints on dyke swarms related to the Paraná-Etendeka magmatic province, and subsequent South Atlantic opening, southeastern Brazil. *J. Volcanol. Geotherm. Res.* **80**, 67–83.

Deino, A.L. (2012) Mass Spec – version 7.884 – Program documentation. Berkeley Geochronology Center.

Deng Y., Ren J., Guo Q., Cao J., Wang H. and Liu C. (2017) Rare earth element geochemistry characteristics of seawater and porewater from deep sea in western Pacific. *Sci. Rep.* **7**, 16539.

Elderfield H. (1988) The oceanic chemistry of the rare-earth elements. Philos. Transact. R. Soc. London, Series A. *Math. Phys. Sc.* **325**, 105–126.

Ewart A., Milner S. C., Armstrong R. A. and Duncan A. R. (1998) Etendeka volcanism of the Goboboseb Mountains and Messum Igneous Complex, Namibia. *J. Petrol.* **39**(2), 191–225.

Farias F., Szatmari P., Bahniuk A. and França A. B. (2019) Evaporitic carbonates in the pre-salt of Santos Basin – Genesis and tectonic implications. *Marine Petrol. Geol.* **105**, 251–272.

Fernandes L. B. M., Sá E. F. J., Vasconcelos P. M. P. and Córdoba V. C. (2020) Structural controls and 40Ar/39Ar geochronological data of basic dike swarms in the eastern domain of the Parnaíba Basin, northeast Brazil. *J. South Am. Earth Sci.* **101** 102601.

Ferroni F. R., Mello C. L. and Destro N. (2017) Tectonic control on the Cabo Frio anorogenic magmatic lineament, Southeastern Brazil. *J. South Am. Earth Sci.* **83**, 37–54.

Fleck R. J., Sutter J. F. and Elliot D. H. (1977) Interpretation of discordant 40Ar/39Ar age-spectra of Mesozoic tholeiites from Antarctica. *Geochim. Cosmochim. Acta* **41**, 15–32.

Florisbal L. M., Heaman L. M., Janasi V. A. and Bitencourt M. F. (2014) Tectonic significance of the Florianopolis Dyke Swarm, Parana-Etendeka Magmatic Province: a reappraisal based on precise U-Pb dating. *J. Volcanol. Geotherm. Res.* **289**, 140–150.

Gomes C. B., Azzone R. G., Ruberti E., Vasconcelos P. M., Sato K. and Rojas G. E. E. (2018) New age determinations for the Banhadão and Itapirapuã complexes in the Ribeira Valley, southern Brazil. *Braz. J. Geol.* **48**(2), 403–414.

Gomes A. S. and Vasconcelos P. M. (2021) Geochronology of the Paraná-Etendeka large igneous province. *Earth Sci Rev.* **220** 103716.

Granot R. and Dyment J. (2015) The Cretaceous opening of the South Atlantic Ocean. *Earth Planet. Sci. Lett.* **414**, 156–163.

Guedes E., Heilbron M., Vasconcelos P. M., de Morisson Valeriano C., Horta de Almeida J. C., Teixeira W. and Filho A. T. (2005) K-Ar and $^{40}Ar/^{39}Ar$ ages of dikes emplaced in the onshore basement of the Santos Basin, Resende area, SE Brazil: Implications for the south Atlantic opening and Tertiary reactivation. *J. South Am. Earth Sci.* **18**, 371–382.

Guedes E., Heilbron M., de Morisson Valeriano C., de Almeida J. C. H. and Szatmari P. (2016) Evidence of Gondwana early rifting process recorded by Resende-Ilha Grande Dike Swarm, southern Rio de Janeiro, Brazil. *J. South Am. Earth Sci.* **67**, 11–24.

Kempe U., Seltmann R., Graupner T., Rodionov N., Sergeev S. A., Matukov D. I. and Kremenetsky A. A. (2015) Concordant U-Pb SHRIMP ages of U-rich zircon in granitoids from the Muruntau gold district (Uzbekistan): Timing of intrusion, alteration ages, or meaningless numbers. *Ore Geol. Rev.* **65**(1), 308–326.

Kuiper K. F., Deino A., Hilgen F. J., Krijgsman W., Renne P. R. and Wijbrans J. B. (2008) Synchronizing rock clocks of Earth history. *Sci.* **320**, 500–504.

Lavecchia A., Clark S. R., Beekman F., Cloetingh S. A. P. L. and Burov E. (2016) Thermal perturbation, mineral assemblages, and rheology variations induced by dyke emplacement in the crust. *Tectonics* **35**, 1137–1152.

Lee J.-Y., Marti K., Severinghaus J. P., Kawamura K., Yoo H.-S., Lee J. B. and Kim J. S. (2006) A redetermination of the isotopic abundances of atmospheric Ar. *Geochim. Cosmochim. Acta* **70**, 4507–4512.

Le Maitre R., Streckeisen A., Zanettin B., Le Bas M., Bonin B. and Bateman P. (2002) *Igneous Rocks: A Classification and Glossary of Terms: Recommendations of the International Union of Geological Sciences Subcommission on the Systematics of Igneous Rocks*, 2nd ed. Cambridge University Press, Cambridge.

Lima B. E. M., Tedeschi L. R., Pestilho A. L. S., Santos R. V., Vazquez J. C., Guzzo J. V. P. and De Ros L. F. (2020) Deep-burial hydrothermal alteration of the Pre-Salt carbonate reservoirs from northern Campos Basin, offshore Brazil: Evidence from petrography, fluid inclusions, Sr, C and O isotopes. *Marine Petrol. Geol.* **113** 104143.

Machado F. B., Rocha-Júnior E. R. V., Marques L. S. and Nardy A. J. R. (2015) Volcanological aspects of the northwest region of Paraná continental flood basalts (Brazil). *Solid Earth* **6**, 227–241.

Magee C., Pichel L. M., Madden-Nadeau A. L., Jackson C.-A.-L. and Mohriak W. (2021) Salt–magma interactions influence intrusion distribution and salt tectonics in the Santos Basin, offshore Brazil. *Basin Res.* **00**, 1–24.

Marques L. S., DeMin A., Rocha-Júnior E. R. V., Babinski M., Bellieni G. and Figueiredo A. M. G., et al. (2018) Elemental and Sr-Nd-Pb isotope geochemistry of the Florianópolis Dyke Swarm (Paraná Magmatic Province): crustal contamination and mantle source constraints. *J. Volcanol. Res.* **355**, 149–164.

Marques L. S., Dupre B. and Piccirillo E. M. (1999) Mantle source compositions of the Paraná Magmatic Province: evidence from trace element and Sr-Nd-Pb isotope geochemistry. *J. Geodyn.* **28**, 439–459.

Marques L. S., Rocha-Júnior E. R. V., Babinski M., Carvas K. Z. C., Petronilho L. A. and De Min A. (2016) Lead isotope constraints on the mantle sources involved in the genesis of Mesozoic high-Ti tholeiite dykes (Urubici type) from the São Francisco Craton (Southern Espinhaço, Brazil). *Braz. J. Geol.* **46**(1), 105–122.

Marzoli A., Melluso L., Morra V., Renne P., Sgrosso I., D'Antonio M., Duarte Morais L., Morais E. A. A. and Ricci G. (1999) Geochronology and petrology of cretaceous basaltic magmatism in the Kwanza basin (Western Angola), and relationships with the Parana-Etendeka continental flood basalt province. *J. Geodyn.* **28**, 341–356.

McDonough W. F. and Sun S. (1995) The composition of the Earth. *Chem. Geol.* **120**, 223–253.

McDougall I. and Harrison T. M. (1999) *Geochronology and Thermochronology by the $^{40}Ar/^{39}Ar$ method*. Oxford University Press, England.

Montes-Lauar C. R., Pacca I. G., Melfi A. J. and Kawashita K. (1995) Late Cretaceous alkaline complexes, southeastern Brazil: Paleomagnetism and geochronology. *Earth Planet. Sci. Lett.* **134**(3–4), 425–440.

Milani, E., Filho, A (2000) Sedimentary basins of South America, in: Cordani, U.G., Milani, E.J., Thomaz Filho, A., Campos, D. A. (Eds.), Tectonic evolution of South America. Internatl. Geol. Congr. 31: 389–449.

Mizusaki A. M. P., Petrini R., Bellieni G., Comin-Chiaramonti P., Dias J., De Min A. and Piccirillo E. M. (1992) Basalt magmatism along the passive continental margin of SE Brazil (Campos Basin). *Contrib. Mineral. Petrol.* **111**, 143–160.

Nardy A. J. R., Oliveira M. A. F. and Figueiredo A. M. (1997) Geoquímica das Rochas Vulcânicas Ácidas Mesozóicas da Região Central da Bacia do Paraná. *V Simp. Geol.* **S.E**, 65–67.

Oreiro S. G., Cupertino J. A., Szatmari P. and Filho A. T. (2008) Influence of pre-salt alignments in post-Aptian magmatism in the Cabo Frio High and its surroundings, Santos and Campos basins, SE Brazil: An example of non-plume-related magmatism. *J. South Am. Earth Sci.* **25**(1), 116–131.

Paton C., Hellstrom J., Paul B., Woodhead J. and Hergt J. (2011) Iolite: freeware for the visualisation and processing of mass spectrometric data. *J. Anal. At. Spectrom.* **26**(12), 2508–2518.

Peate, D.W. (1997) The Paraná-Etendeka Province, in: Mahoney, J.J., Coffin, M. (Eds.), Large Igneous Provinces. Am. Geophys. Union, Geophys. Monogr. Ser. 100, pp. 217–245.

Peate D. W., Hawkesworth C. J. and Mantovani M. S. M., et al. (1992) Chemical stratigraphy of the Paraná lavas, South America: classification of magma types and their spatial distribution. *Bul. Volcanol.* **55**, 119–139.

Peixoto C. A., Heilbron M., Ragatky D., Armstrong R., Dantas E., Valeriano C. M. and Simonetti A. (2017) Tectonic Evolution of the Juvenile Tonian Serra da Prata magmatic arc in the Ribeira Belt, SE Brazil: Implications for early west Gondwana amalgamation. *Precambrian Res.* **302**, 221–254.

Petrus J. A., Chew D. M., Leybourne M. I. and Kamber B. S. (2017) A new approach to laser-ablation inductively-coupled-plasma mass spectrometry (LA-ICP-MS) using the flexible map interrogation tool 'Monocle'. *Chem. Geol.* **463**, 76–93.

Piccirillo E. M. and Melfi A. J. (1988) *The Mesozoic flood volcanism of the Paraná Basin: petrogenetic and geophysical aspects*. Universidade de São Paulo, São Paulo, Instituto Astronômico e Geofísico.

Raposo M. I. B., Ernesto M. and Renne P. R. (1998) Paleomagnetism and 40Ar/39Ar dating of the Early Cretaceous Flo-

rianópolis dike swarm (Santa Catarina Island), Southern Brazil. *Phys. Earth Planet. Inter.* **108**, 275–290.

Ren Z. and Vasconcelos P. M. (2019) Argon diffusion in hypogene and supergene alunites: implications to geochronology and thermochronometry on Earth and Mars. *Geochim. Cosmochim. Acta* **262**, 166–187.

Renne P. R., Mertz D. F., Ernesto M., Marques L. S., Teixeira W., Ens H. H. and Richards M. A. (1993) Geochronologic constraints on magmatic and tectonic evolution of the Paraná Province. *EOS, AGU* **26**, 553.

Renne P. R., Glen J. M., Milner S. C. and Duncan A. R. (1996) Age of Etendeka flood volcanism and associated intrusions in southwestern Africa. *Geol.* **24**, 659–662.

Renne P. R., Swisher C. C., Deino A. L., Karner D. B., Owens T. L. and DePaolo D. J. (1998) Intercalibration of standards, absolute ages and uncertainties in 40Ar/39Ar dating. *Chem. Geol.* **145**, 117–152.

Rivalta E., Taisne B., Bunger A. P. and Katz R. F. (2015) A review of mechanical models of dike propagation: Schools of thought, results and future directions. *Tectonophys.* **638**, 1–42.

Rocha-Júnior E. R. V., Marques L. S., Babinski M., Nardy A. J. R., Figueiredo A. M. G. and Machado F. B. (2013) Sr-Nd-Pb isotopic constraints on the nature of the mantle sources involved in the genesis of the high-Ti tholeiites from Northern Paraná Continental Flood Basalts (Brazil). *J. South Am. Earth Sci.* **46**, 9–25.

Rocha-Júnior E. R. V., Marques L. S., Babinski M., Machado F. B., Petronilho L. A. and Nardy A. J. R. (2020) A telltale signature of Archean lithospheric mantle in the Paraná continental flood basalts genesis. *Lithos*, 364–365.

Schaen A. J., Jicha B. R., Hodges K. V., Vermeesch P., Stelten M. E., Mercer C. M., Phillips D., Rivera T. A., Jourdan F., Matchan E. L., Hemming S. R., Morgan L. E., Kelley S. P., Cassata W. S., Heizler M. T., Vasconcelos P. M., Benowitz J. A., Koppers A. A. P., Mark D. F., Niespolo E. M., Sprain C. J., Hames W. E., Kuiper K. F., Turrin B. D., Renne P. R., Ross J., Nomade S., Guillou H., Webb L. E., Cohen B. A., Calvert A. T., Joyce N., Ganerød M., Wijbrans J., Ishizuka O., He H., Ramirez A., Pfänder J. A., Lopez-Martínez M., Qiu H. and Singer B. S. (2020) Interpreting and reporting 40Ar/39Ar geochronologic data. *GSA Bull.* **133**(3–4), 461–487.

Schmitt R. S., Trouw R. A. J., Van Schumus W. R. and Pimentel M. M. (2004) Late amalgamation in the central part of West Gondwana: new geochronological data and the characterization of a Cambrian collisional orogeny in the Ribeira Belt (SE Brazil). *Precambrian Res.* **113**, 29–61.

Schmitt R. S., Trouw R., Van Schmus W. R., Armstrong R. and Stanton N. S. G. (2016) The tectonic significance of the Cabo Frio Tectonic Domain in the SE Brazilian margin: a Paleoproterozoic through Cretaceous saga of a reworked continental margin. *Braz. J. Geol.* **46**(1), 37–66.

Sharp D. W. and Renne P. R. (2005) The 40Ar/39Ar dating of core recovered by the Hawaii Scientific Drilling Project (phase 2), Hilo, Hawaii. *Geochem. Geophys. Geosyst.* **6**(4), Q04G17.

Spell T. L. and McDougall I. (2003) Characterization and calibration of 40Ar/39Ar dating standards. *Chem. Geol.* **198**, 189–211.

Stanton N., Schmitt R. S., Galdeano A., Maia M. and Mane M. (2010) Crustal Structure of the Southeastern Brazilian Margin, Campos Basin, from Aeromagnetic Data: New kinematic constraints. *Tectonophys.* **490**, 15–27.

Thiede D. S. and Vasconcelos P. M. (2010) Parana flood basalts: Rapid extrusion hypothesis confirmed by new 40Ar/39Ar results. *Geol.* **38**(8), 747–750.

Thybo H. and Nielsen C. (2009) Magma-compensated crustal thinning in continental rift zones. *Nat.* **457**, 873–876.

Turner S., Regelous M., Kelley S., Hawkesworth C. and Mantovani M. (1994) Magmatism and continental break-up in the South Atlantic: high precision 40Ar39Ar geochronology. *Earth Planet. Sci. Lett.* **121**, 333–348.

Thompson R. N., Gibson S. A., Mitchell J. G., Dickin A. P., Leonardos O. H., Brod J. A. and Grennwood J. C. (1998) Migrating Cretaceous-Eocene magmatism in the Serra do Mar Alkaline Province, SE Brazil: melts from the deflected Trindade mantle plume? *J. Petrol.* **39**, 1493–1526.

Thompson R. N., Gibson S. A., Dickin A. P. and Smith P. M. (2001) Early Cretaceous basalt and picrite dykes of the southern Etendeka region, NW Namibia: windows to the role of the Tristan mantle plume in Paraná-Etendeka magmatism. *J. Petrol.* **11**, 2049–2081.

Ubide T., McKenna C. A., Chew D. M. and Kamber B. S. (2015) High-resolution LA-ICP-MS trace element mapping of igneous minerals: In search of magma histories. *Chem. Geol.* **409**, 157–168.

Ubide T., Mollo S., Zhao J., Nazzari M. and Scarlato P. (2019) Sector-zoned clinopyroxene as a recorder of magma history, eruption triggers, and ascent rates. *Geochim. Cosmochim. Acta* **251**, 265–283.

Ures U., Bossi J., Féraud G. and Bertrand H. (1997) New Age and Geochemical Constraints on the Paraná Flood Volcanism: Additional Data on Uruguay Extrusive and Intrusive Formations. *AGU Fall mtg.* **VI**, E-11.

Vasconcelos P. M., Knesel K. M., Cohen B. E. and Heim J. A. (2008) Geochronology of the Australian Cenozoic: a history of tectonic and igneous activity weathering, erosion, and sedimentation. *Aus. J. Earth Sci.* **55**(6–7), 865–914.

Veizer J. (1989) Strontium isotopes in seawater through time. *Ann. Rev. Earth Planet. Sci.* **17**, 141–167.

Verati C. and Jourdan F. (2014) Modelling effect of sericitization of plagioclase on the 40 K/40Ar and 40 Ar/39 Ar chronometers: implication for dating basaltic rocks and mineral deposits. *Geol. Soc. London Spec. Publ.* **378**, 155–174.

Warren J. K. (2016) *Evaporites – A Geological Compendium*. Springer, Switzerland.

Zheng X., Plancherel Y., Saito M. A., Scott P. M. and Henderson G. M. (2016) Rare earth elements (REEs) in the tropical South Atlantic and quantitative deconvolution of their non-conservative behavior. *Geochim. Cosmochim. Acta* **177**, 217–237.

Associate editor: Fred Jourdan